Desalination 492 (2020) 114596

Contents lists available at ScienceDirect

Desalination

journal homepage: www.elsevier.com/locate/desal

Bacterial-cellulose-derived carbonaceous electrode materials for water desalination via capacitive method: The crucial role of defect sites

Yolanda Belaustegui[a], Fabiola Pantò[b], Leire Urbina[c], Maria Angeles Corcuera[c], Arantxa Eceiza[c], Alessandra Palella[b], Claudia Triolo[d,*], Saveria Santangelo[d,*]

[a] Tecnalia, Basque Research and Technology Alliance (BRTA), Materials for Energy and Environment Area, 48160 Derio, Bizkaia, Spain
[b] Istituto di Tecnologie Avanzate per l'Energia (ITAE) del Consiglio Nazionale delle Ricerche (CNR), 98126 Messina, Italy
[c] Department of Chemical and Environmental Engineering, Engineering School of Gipuzkoa, 'Materials + Technologies' Group, University of the Basque Country (UPV/EHU), 20018 Donostia-San Sebastián, Spain
[d] Dipartimento di Ingegneria Civile, dell'Energia, dell'Ambiente e dei Materiali (DICEAM), Università "Mediterranea", 89122 Reggio Calabria, Italy

ARTICLE INFO

Keywords:
Bacterial cellulose
Raman spectroscopy
Lattice defects
Capacitive deionization

ABSTRACT

Electrosorptive desalination is a very simple and appealing approach to satisfy the increasing demand for drinking water. The large-scale application of this technology calls for the development of easy-to-produce, cheap and highly performing electrode materials and for the identification and tailoring of their most influential properties, as well. Here, biosynthesised bacterial cellulose is used as a carbon precursor for the production of three-dimensional nanostructures endowed with hierarchically porous architecture and different density and type of intrinsic and hetero-atom induced lattice defects. The produced materials exhibit unprecedented desalination capacities for carbon-based electrodes. At an initial concentration of 585 mg L^{-1} (10 mmol L^{-1}), they are able to remove from 55 to 79 mg g^{-1} of salt; as the initial concentration rises to 11.7 g L^{-1} (200 mmol L^{-1}), their salt adsorption capacity reaches values ranging between 1.03 and 1.35 g g^{-1}. The results of the thorough material characterisation by complementary techniques evidence that the relative amount of oxygenated surface functional species enhancing the electrode wettability play a crucial role at lower NaCl concentrations, whereas the availability of active non-sp^2 defect sites for adsorption is mainly influential at higher salt concentrations.

1. Introduction

The availability of drinking water is becoming inadequate to satisfy the ever growing demand caused by the increase of world population, enhancement of environmental pollution level and climate changes. According to the estimation by the United Nations, more than one billion people currently live in water-stressed regions and this situation will worsen in the next years, with almost half the world's population expected to live in areas of high water-stress by 2030 [1]. Water shortage is aggravated in Countries where the necessary infrastructure to take water from rivers and aquifers lack. Clean water has been recognised as a basic human right by the United Nations [2]. Its availability and affordability are among the main social, technological, and economical challenges to be faced by the World in the 21st century.

Since 97% of the Planet's water is seawater, seawater desalination potentially represents the smart solution to scarcity of fresh water. This has encouraged the development of several water desalination technologies (e.g. reverse osmosis, distillation, electrodialysis) [3]. Among the cost-effective and energy-efficient ones, electrosorptive desalination looks particularly attractive thanks to its simplicity, easy maintenance, low energy consumption and environmental impact. Also known as capacitive de-ionization (CDI), it removes charged ionic species from water via the electrostatic interaction with the two electrodes forming CDI-cell, to which an external voltage is applied [4–7]. Low energy required to desalinate one cubic meter of brackish waters (approximately only one half compared to reverse osmosis [8]) and low operating voltage of the cell ($\leq$ 2 V) makes CDI economically competitive and strategically important for areas without electricity grid.

Although several factors (e.g. cell design and operational settings) strongly influence the CDI performance, physical and structural properties of the porous electrode materials represent a key point. Besides high surface area, electronic conductivity, electrochemical stability and wettability, also the total volume, average size and connectivity of the pores are important, which has made carbon the material of most frequent choice for developing and fabricating porous electrodes [6,7]. A wide variety of reports on nanocarbons is available in the literature

* Corresponding authors.
E-mail addresses: claudia.triolo@unirc.it (C. Triolo), saveria.santangelo@unirc.it (S. Santangelo).

https://doi.org/10.1016/j.desal.2020.114596
Received 1 May 2020; Received in revised form 19 June 2020; Accepted 25 June 2020

[9–11]. Although endowed with good CDI performance, many of them suffer from relatively complicated manufacturing processes and high production cost. The search for new highly performing materials with low cost and easy synthesis routes is crucial for the development and the practical application of the CDI technology.

Bacterial cellulose (BC) is the most abundant lignin-free biopolymer in nature [12,13]. Although it exhibits the same chemical structure as plant-derived cellulose, $(C_6H_{10}O_5)_n$, BC is endowed with higher crystallinity, water-holding capacity, mechanical strength, and purity [12,14]. Its synthesis occurs in three stages, namely *i*) polymerization of the glucose into long and unbranched chains (β-1,4-D-glucan) linked with hydrogen bonding; assembly of *ii*) several protofibrils, consisting of a few of parallel chains, into 2–4 nm-wide nanofibrils, and *iii*) of bundles of nanofibrils into 20–100 nm-wide nanoribbons, finally giving rise to a three-dimensional (3D) network of interwoven randomly-oriented nanoribbons (BC pellicle) [12,15]. Owing to interfibrillar voids at the various scales, the 3D cellulosic architecture is endowed with hierarchical porosity.

This extracellular biopolymer is biosynthesised through the pores of the membrane of some bacterial strains including those belonging to genera *Rhizobium, Gluconacetobacter, Agrobacterium, Sarcina* and *Alcaligenes*. Among bacteria able to secrete bundles of cellulose chains as part of their metabolism, *Gluconacetobacter* is the genus with the highest BC production ability [15]. Classified in the family *Acetobacteraceae*, it contains several strains, including *Gluconacetobacter xylinus* the most studied among them [12–18]. Recently, *Gluconacetobacter medellinensis* (ID13488), a strain isolated from homemade fruit vinegar in Medellin (Colombia) central market, has gathered great attention due to its ability to produce crystalline BC under highly acidic conditions, as desirable for industrial production from acidic residues (e.g. wastes generated from cider production) [19].

Due to its interesting conformation, biocompatibility and biodegradability, BC has attracted attention in a wide range of new applications in the biomedical field [20–22], such as tissue engineering [23], drug delivery and wound dressing [24,25], in the food packaging area [26,27] and also in environmental applications [28].

Moreover, thanks to its wide availability (BC is biosynthesized on a scale of several billion tons per year [29]), in the last decades, it has been extensively exploited as a cheap and green carbon source for the production of a variety of carbon-based materials [30], most frequently utilised in the field of energy storage. Several works are available in the literature dealing with BC-derived electrode materials for supercapacitors [31–40] and rechargeable batteries [41–43]. However, recently, the use of BC-derived carbon-based materials has been reported also for different interesting applications, such as capacitive deionization [44], absorption of oils and organic solvents [45], electromagnetic interference shielding [46].

In this work, BC is utilised as a carbon precursor for the preparation of electrode materials for the desalination of water via the capacitive method. The electrochemical performance of the BC-derived nanocarbons is evaluated. The effect of the enrichment with graphene is also investigated. The outstanding results obtained in terms electrosorptive performance are correlated with the microstructural properties of the electrode materials, as described by micro-Raman spectroscopy, and the crucial role of the carbon defects is emphasised.

2. Experimental

2.1. Preparation of the pristine materials

2.1.1. Pure BC

Gluconacetobacter medellinensis strain ID13488 (CECT 8140) was used for the biosynthesis of BC membranes. Bacterial cells were grown, for 14 days under static conditions, in a standard Hestrin-Schramm (HS) medium containing D-glucose (2% w/v), peptone (0.5% w/v), yeast extract (0.5% w/v), disodium hydrogen phosphate (0.27% w/v) and citric acid (0.115% w/v). The incubation temperature and pH of the medium were 28 °C and 4, respectively The obtained BC membranes were treated with KOH (2 wt%) for 24 h at room temperature (RT) with the dual purpose of *i*) removing non-cellulosic compounds and *ii*) generating sub-micropores and defects in the carbonaceous matrix upon carbonisation [47]. Finally, they were freeze-dried (Fig. S1a).

2.1.2. Graphene-enriched BC

In order to investigate the effect of the enrichment of the electrode material with graphene, a composite cellulose/reduced graphene oxide (rGO/BC) membrane was further prepared. This was accomplished via ex-situ instead of in-situ method because of the tendency of GO to precipitate in the culture medium giving rise to a non-homogenous dispersion within the growing matrix. As sketched in Fig. S2, the membranes were immersed in a graphene oxide (GO) suspension for 24 h under sonication. A commercial suspension of GO in water (4 mg mL^{-1}) supplied by Graphenea (average particle size < 10 μm; carbon: 49–56%; oxygen: 41–50%; nitrogen: 0–1%) was used. The obtained membranes were dried in an oven at 50 °C for 24 h between Teflon molds and the resulting GO/BC "paper" was finally chemically reduced to rGO/BC with ascorbic acid (30 g L^{-1}) in an oven for 2 h at 95 °C (Fig. S1b).

Hereafter, the pure BC membrane and the composite rGO/BC "paper" will be labelled as samples p-BC and p-GBC.

2.2. Preparation of the BC-derived carbonaceous materials

In order to obtain carbonaceous materials for the preparation of the electrodes for the CDI cell, the pristine samples were processed as described in detail below and summarised in Table 1.

Following Liu et al. [44], a two-step heating process was carried out on sample p-BC. The process consisted of i) an oxidative treatment (polymer stabilisation) in static air and ii) an annealing (carbonisation) performed at 700 °C under 5.5 purity nitrogen (100 cc min^{-1} flow rate). Based on the results of the thermo-gravimetric analysis (see Fig. S3 in the supporting information), stabilisation was operated at 225 °C. Stabilisation- and carbonisation-temperatures were reached by 5 °C min^{-1} heating rate and kept constant for 2 h. Uncontrolled cooling down to RT followed both the thermal treatments. In the following, the pure-BC derived active material will be labelled as sample BC(N_2).

In order to investigate the effect of the enrichment of the carbonaceous electrode materials with graphene, three composite samples were prepared (Table 1). The first one, below coded as GBC(N_2), was obtained by carbonisation of the rGO-containing p-GBC (Fig. S2). The heat process was operated at 700 °C for 2 h under 100 cc min^{-1} N_2

Table 1
Codes of the pristine and processed samples, with details about their preparation.

Code	Material type and preparation details		
p-BC	Pristine	Pure BC membrane by biosynthesis and freeze-drying	
p-GBC		Composite rGO/BC "paper" by biosynthesis, immersion in GO suspension, molding and chemical reduction	
BC(N_2)	Processed	Graphene-free BC-derived carbon	By stabilisation in air and carbonisation of p-BC in N_2
GBC(N_2)		Graphene-enriched BC-derived carbon	By carbonisation of p-GBC in N_2
BCG(N_2)			By stabilisation in air of p-BC, impregnation with diluted GO suspension and carbonisation in N_2
BCG(He)			By stabilisation in air of p-BC, impregnation with diluted GO suspension and carbonisation in He

flow.

Two additional samples, hereafter labelled as BCG(N_2) and BCG(He), were produced as sketched in Fig. S2 for the former. BCG(N_2) and BCG(He) were prepared by stabilising p-BC in air at 225 °C, impregnating the stabilised material with a diluted GO-suspension and, after drying overnight, carbonising the resulting material at 700 °C for 2 h under 100 cc/min N_2 or He flow, respectively. A commercial suspension of GO in water (Graphenea; 4 mg mL^{-1}), diluted in (¼ v/v) in distilled water (Merck), was used for the impregnation.

2.3. Physicochemical characterisation of pristine and processed materials

The pristine and processed materials were thoroughly characterised. The morphological analysis was performed by scanning electron microscopy (SEM) by utilising a FEI S-FEG XL30 microscope equipped with an energy-dispersive X-ray (EDX) spectrometer. A NETZSCH STA 449C instrument was used for the thermo-gravimetric analysis (TGA). Few milligrams of the sample were loaded in an alumina crucible. The analysis was carried out in air. The 20–800 °C range was investigated rising temperature at a rate of 10 °C min^{-1}. The Brunauer-Emmett-Teller (BET) method was used for the specific surface area determination by using ASAP 2010 Micromeritics equipment. Further details on the sample preparation and experimental data processing can be found elsewhere [11]. X-ray diffraction (XRD) patterns were recorded on a Panalytical X-Pert diffractometer using a Ni β-filtered Cu-K_α radiation (λ = 1.5451 Å) source. Data were collected in the 5–80° 2θ-angle range with a step of 0.05°. Raman scattering excited by a solid-state laser operating at 532 nm (2.33 eV) was measured by using a NT-MDT NTEGRA - Spectra SPM spectrometer equipped with MS3504i 350 mm monochromator and ANDOR Idus CCD. The scattered light from the sample, collected via a Mitutoyo 100× objective, was dispersed by a 600 lines mm^{-1} grating. In order to prevent local heating and annealing effects, a laser power of 250 μW at the sample surface was used. The spatial homogeneity of the samples was further evaluated by recording spectra from several random positions on each specimen and, in order to have a reliable picture of the entire sample, the spectra collected in each specimen were averaged. X-ray photoelectron spectroscopy (XPS) analysis was carried out with a Physical Electronics GMBH PHI 5800-01 spectrometer, equipped with a monochromatic Al-K_α (1486.6 eV) source set at a power beam of 300 W. Spectra were acquired using pass energies of 11.0 eV and 58.0 eV for elemental analysis and determination of the oxidation states, respectively. The binding energy regions of C 1*s*-K 1*s* (280–300 eV), N 1*s* (390–406 eV), and O 1*s* (520–540 eV) were examined, taking the C 1*s* line (284.5 eV) as reference [48]. XPS data were interpreted by using the on-line library of oxidation states implemented in the PHI MULTIPAK 6.1 software and the PHI Handbook of XPS [49]. The elemental concentrations were estimated from the areas under the photoelectron peaks weighed by the relative sensitivity factors. The results obtained are reported in Table 2. For further details on the instrumentation and experimental data processing see refs [11, 50].

Table 2
Surface composition of the samples, as inferred from the XPS analysis.

Code	Atomic concentration/at.%			O/C ratio	Relative weight/wt%		
	C	N	O		C	N	O
BC(N_2)[a]	59.3	0.0	40.7	0.69	52.2	0.0	47.8
GBC(N_2)	71.5	1.9[b]	26.6	0.37	65.5	2.0[b]	32.5
BCG(N_2)[a]	59.0	0.0	41.0	0.69	51.9	0.0	48.1
BCG(He)[a]	52.9	0.0	47.1	0.89	45.6	0.0	54.2
Mixture[c]	62.4	0.5	37.2	0.60	55.5	0.5	44.8

[a] Net values after subtraction of K atomic concentration.
[b] From GO.
[c] Values calculated from the data of BC(N_2) and GBC(N_2) by using the mass 3:1 ratio.

Table 3
Codes of the working electrodes and active materials utilised for their preparation.

Code	Active material(s) and relative code(s)
BCE-0	BC-derived carbon BC(N_2)
BCE-1	3:1[a] mixture of BC-derived carbon BC(N_2) and graphene-enriched BC-derived carbon GBC(N_2)
BCE-2	Graphene-enriched BC-derived carbon BCG(He)
BCE-3	Graphene-enriched BC-derived carbon BCG(N_2)

[a] The 3:1 mass ratio was chosen in order to obtain comparable GO contents of the three graphene-enriched electrodes (~5 wt%).

2.4. Preparation of the working electrodes based on the BC-derived carbonaceous materials

Four working electrodes were prepared by using the thermally processed BC-derived carbonaceous materials. Their codes are reported in Table 3. Three of them (BCE-1, BCE-2 and BCE-3) were based on graphene-enriched samples; in the case of BCE-1, a physical mixture of samples GBC(N_2) and BC(N_2) in a 1:3 mass ratio was used as an active material. The electrodes were prepared via the procedure previously described in detail [11,50]. Briefly, the active material (90 wt%) was mixed with polyvinylalcohol (10 wt%), supplied by Tecnalia, and the resulting mixture was dispersed in ethanol. The slurry obtained after 8 h stirring was cast onto the (Mersen Iberica) graphite current collector and dried in an oven at 60 °C overnight.

2.5. Electrochemical three-cell measurements

A conventional three-electrode system, using a computer-controlled AUTOLAB PGSTAT302N Metrohm potentiostat/galvanostat, was utilised to carry out cyclic voltammetry (CV) measurements. The working electrode was prepared as-described in Section 2.4; graphite acted as the counter electrode, while a standard Ag/AgCl electrode was used as the reference. CV measurements were carried out at RT in 0.1 mol L^{-1} NaCl solution at different scan rates (5, 10, 20, 30, 40, 50 and 100 mV s^{-1}); the potential range from −1.3 to 0.4 V was investigated. The specific capacitance, C_S (F g^{-1}), was calculated from the current-voltage curves as

$$Cs = \frac{1}{vm}\int \frac{I}{V}\,dV, \tag{1}$$

where I (A), V (V), v (V s^{-1}) and m (g) denote the response current, the potential, the potential scan rate and the mass of the electro-active material [11].

Electrochemical impedance spectroscopy (EIS) analysis was carried out in the $1{\cdot}10^{-1}$-$1{\cdot}10^{4}$ Hz frequency range with AUTOLAB PGSTAT302N using the three-compartment cell (amplitude of the alternating voltage: $1{\cdot}10^{-1}$ V around the 0 V equilibrium potential).

Area of the working electrodes utilised for CV ad EIS measurements was 2 cm^2. Further details can be found elsewhere [11,50].

2.6. Electrosorption experiments

Batch mode experiments in a continuously recirculating system were carried out to investigate the electrosorption behaviour of the BC-derived electrodes. The system, previously described [11], included a symmetric electrosorptive unit cell, two reservoirs, a peristaltic Fisher Scientific, Mini-pump, a Hanna Microprocessor Conductivity/TDS meter and a DC Lab Power supply LABPS1503. Area of the two parallel electrodes forming the CDI unit cell was 9 cm^2; a non-electrically conductive separator was interposed between them. 100 mL of NaCl solution, kept at 25 °C, were utilised in each experiment (flow rate:

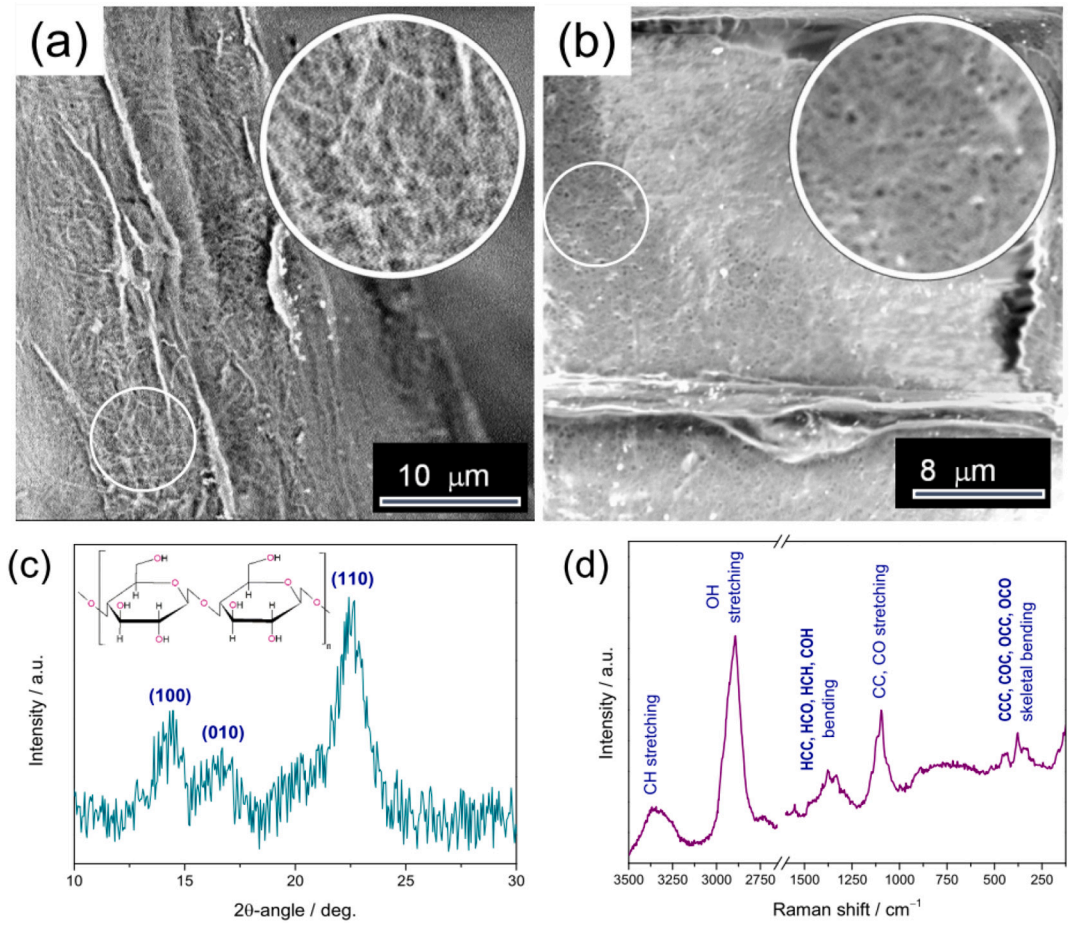

Fig. 1. Results of (a–b) SEM, (c) XRD and (d) MRS analyses on sample p-BC.

7.7 mL min^{-1}). A 1.2 V voltage was applied until the complete cell charging and equilibrium concentration were reached [11,51].

The salt adsorption capacity, *SAC* (mg g^{-1}), was calculated as

$$SAC = \frac{(C_0 - C_t)\tau}{m}, \quad (2)$$

where C_0 (mg L^{-1}) and C_t (mg L^{-1}) stand for the initial and the instantaneous equilibrium-concentrations, respectively; τ (L) and m (g) indicate the solution volume and the mass of the (active) electrode pair, respectively. To check the reproducibility, several experiments were carried out on each type of electrode material, and the corresponding *SAC* was calculated averaging over the values obtained in these experiments.

3. Results and discussion

3.1. Physicochemical properties of the pristine pure BC and composite GBC samples

Figs. 1 and S4–S5 summarise the results of SEM/EDX, XRD and micro-Raman spectroscopy (MRS) analyses on the freeze-dried BC. Fig. 1a–b shows representative SEM images of the samples; lower-magnification images can be found in the supporting information (SI, Fig. S4a–b). The highly-porous fibrillar-net-like morphology, peculiar to biosynthesised cellulose [52], is clearly visible. Bundles of microfibrils, densely-packed due to the water removal process [13], can be observed, along with numerous macropores (in both the image insets). The randomly-oriented microfibrils are interconnected to form a 3D cellulosic skeleton, featured by hierarchical porosity. The analysis at higher magnification factors reveals the lack of spatial uniformity in terms of length and thickness of the microfibrils and bundles, as well. Conversely, the elemental mapping via SEM/EDX (Fig. S4c) evidences a spatially homogeneous distribution of carbon, oxygen, potassium (deriving from treatment in KOH) at the micro-scale.

Native cellulose I is composed of I_α and I_β allomorphs. The two phases have the same molecular building and O_3–H–O_5 intra-chain hydrogen bonding, but different O_2–H–O_6 inter-chain hydrogen bonding and crystal structure [17]. Their relative amount depends on the source of the cellulose [17,53]. In general, plant-derived cellulose is rich in I_β allomorph, while I_α is the predominant allomorph in cellulose derived from algae and bacteria. Three diffraction peaks are detected in the XRD pattern of p-BC around 14.5°, 16.6° and 22.6° (Fig. 1c). These major reflections correspond to (100), (010), (110) planes in the I_α phase, and (1 − 10), (110), (200) in the I_β one. In this case, the diffraction patterns have been indexed according to Miller indexes of cellulose I_α, the predominant allomorph in p-BC [53].

The crystallinity index of the freeze-dried BC was estimated, via the empirical formula $\chi = 100 \cdot [I_{(110)} - I_A]/I_{(110)}$, proposed by Segal et al. [54,55], where $I_{(110)}$ denotes the intensity of the main diffraction peak at 22.6° of I_α phase and I_A indicates the intensity due to the amorphous contribution at 18° 2θ-angle. The mean crystallite size was calculated, from the full width at half maximum (FWHM) of the (110) peak, through the Scherrer's equation, $d_{BC} = k\lambda/\beta\cos\theta$, where k (0.89) is the shape factor, λ is the wavelength of x-ray radiation, β is the FWHM in radians and θ is the Bragg's angle [16]. Despite the relatively low signal-to-noise ratio of the pattern, the found χ- and d_{BC}-values (85 ± 5% and 6.1 ± 0.3 nm, respectively) were comparable with those reported in the literature for the cellulose produced from HS medium [16,56].

The measure of Raman scattering from different random locations in

the freeze-dried BC (Fig. S5) pointed at the lack of spatial uniformity within the sample, reflecting the local changes in the morphology (Fig. 1a–b) and in the crystallinity degree [17,35]. Thus, in order to have a reliable picture of the entire sample, the spectra relative to the different locations sampled were averaged. Fig. 1d shows the result obtained. The spectral profile is peculiar to cellulose I [17,57]. The skeletal bending modes of CCC, COC, OCC, OCO bonds are detected in the lowest frequency region of the spectrum (150–550 cm^{-1}) [17]. The intense stretching modes of CC and CO bonds dominate the 800–1180 cm^{-1} region [17]. At higher frequencies (1180–1430 cm^{-1}), the bending modes of HCC, HCO, HCH and COH bonds contribute to the Raman intensity [17]. Above 2500 cm^{-1}, a very intense band centred at ~2900 cm^{-1} and a weaker and broader one (at ~3350 cm^{-1}) are detected. The former originates from the stretching modes of CH bonds, while the latter is associated to the stretching modes of OH bonds [17]. No cellulose mode contributes to the Raman intensity between 1500 and 2500 cm^{-1}.

The intensities I_{380} and I_{1096} of the Raman bands at 380 and 1096 cm^{-1} were utilised to estimate the crystallinity of the freeze-dried BC via the empirical formula $\chi' = [(I_{380}/I_{1096})\text{-}0.0286]/0.0065$, proposed by Agarwal et al. [58]. The so-obtained χ'-value (70.4%) was comparable with that obtained by the same method for BC nanocrystals [59] and compatible with the crystallinity index inferred from the XRD pattern.

The XRD patterns of composite GO/BC, rGO/BC or graphene/BC samples generally exhibit the same diffraction peaks as pure cellulose [18,32,60–62]; rarely the detection of an additional peak originating from the (001) reflection of graphene oxide has been reported [63]. In the present case, the comparison between the diffractograms of samples p-GBC (not shown) and p-BC (Fig. 1c) evidenced the presence of no extra peak ascribable to rGO. Conversely, only the fingerprint of rGO was clearly visible in the micro-Raman spectrum of p-GBC (Fig. S6), in full agreement with the results reported by other authors [32,60]. Different from the case of pure cellulose, the comparison among spectra from different random locations in the composite sample evidenced a great degree of spatial homogeneity, in full agreement with the literature [18,60,62].

3.2. Physicochemical properties of the BC-derived fibrous electrode materials

Figs. 2 and S7 summarise the results of SEM, MRS, XRD and XPS analyses on the thermally processed samples. Fig. 2a–f shows representative SEM images of the samples; lower-magnification images can be found in the SI (Fig. S7). As expected [36,47], after carbonisation at 700 °C, the 3D architecture of pristine material, resulting from randomly-oriented interconnected cellulosic microfibrils, is preserved and the samples exhibit the morphology featured by hierarchical porosity typical of BC-derived nanocomposites [33] and of high surface-area pyrolysed nanocarbons [31], as well. Moreover, the spatial inhomogeneity observed in pure cellulose reduces to some extent (Figs. 2b,e and S7c).

The D- and G-bands, peculiar to disordered/amorphous graphitic nanocarbons, are detected in the micro-Raman spectra of all the samples (Figs. 2g and S8), which confirms the carbonisation of cellulose. The latter, ascribed to the E_{2g} symmetry stretching of all sp^2 bonded C=C pairs [64], is regarded as the Raman fingerprint of the graphitic ordering. The former, originating from the A_{1g} symmetry in-plane breathing of the aromatic C rings, is disorder-activated [64]. Since its relative (to the G-band) intensity rises with increasing deviation from perfect hexagonally-organised planar carbon network [64,65], the D/G intensity ratio (I_D/I_G) is commonly used to monitor the density of the sp^2-defects in nanocarbons [64,66–68].

Only a slight increase of I_D/I_G is observed by comparing the micro-Raman spectra of samples GBC(N_2) and p-GBC (Fig. S8a), which indicates that the heat treatment at 700 °C on the composite rGO/BC sample does not produce significant structural changes in the carbonaceous matrix. On the contrary, the comparison among the four carbonised samples (Fig. 2g) evidences marked spectral differences. The "disorder-band" appears to be the most affected by the change. Its width increases in the order GBC(N_2) < BCG(N_2) < BCG(He) < BC(N_2). A progressive weakening (relative to the G-band) accompanies the broadening. The G-band broadens too. Its width increases to minor extent, but in the same order as for the D-band. Moreover, the band moves towards higher frequencies. The increase in its frequency position is in the order GBC(N_2) < BC(N_2) < BCG(N_2) < BCG(He).

Since clustering of the sp^2 phase, bond disorder, presence of sp^2 rings or chains, hybridisation changes of the C—C bonding act as competing forces on the shape of the Raman spectra of nanocarbons [64], the described spectral changes point at differences in the microstructure of the samples. As for the D-band, Li et al. [69] reported analogous (not explained) spectral differences for biomass-derived hard carbon micro-spherules obtained via carbonisation at different temperatures. In the case of the micro-spherules, the I_D/I_G ratio increased and the D-band sharpened with increasing carbonisation temperature. The increase of carbonisation temperature produced a similar spectral evolution also in BC-derived carbon fibres [44,46]. Liu et al. [44] ascribed the I_D/I_G increase to the formation of defects. On the contrary, Dai et al. [46] explained the spectral changes in terms of an increase in the crystallite domains or a reduction in the quantity of amorphous carbon.

Indeed, only sp^2 carbon defects contribute to the D-band intensity [64], whereas non-sp^2 ones (trans-poly-acetylene-like chains, formed at the zig-zag edges of the defective graphitic layers and Csp^3 phases interconnecting the graphitic domains) contribute to the Raman intensity at lower and higher frequencies (T-band at 1150–1230 cm^{-1} and A-band at 1450–1530 cm^{-1}, respectively) [70,71]. Thus, the intensifying of the "sp^2-disorder band" moving from sample BC(N_2) to sample GBC(N_2) is here understood as the effect of the increase of the sp^2-defects with respect to the non-sp^2 ones, while the shrinking of the D-and G-bands is thought of as reflecting the evolution towards a narrower distribution of bond angles and lengths, which is consistent with what proposed by Dai et al. [46]. Actually, only sp^2-defects are present in the carbonaceous lattice of GBC(N_2) (Fig. S9), which appears to be the most (graphitically) ordered sample, despite their large density. Conversely, the highest amorphousness degree (i.e. the greatest deviation from perfect Csp^2 network), with large bond (angle and length) disorder and non-sp^2 defects, along with the sp^2-ones, pertains to sample BC(N_2). This is a relevant feature since, as known [44], the presence of defects can generate more accessible surface area and cause an increase in the ability to accumulate charges, which is beneficial for the charge transfer in the adsorption process.

The broad diffraction peaks associated to the reflection from (002) and (101) graphitic planes are clearly visible in the XRD patterns of all the samples (Fig. 2h), confirming the disordered/amorphous nature of the investigated nanocarbons [69,72], as well as the effective thermal reduction of GO. Nevertheless, in sample GBC(N_2), the most intense peak is slightly narrow and located at higher 2θ-angle values with respect to the remaining samples, which supports the conclusions drawn from the analysis of micro-Raman spectra (i.e. it exhibits the highest degree of graphitic ordering). The average interlayer spacing was estimated from the angular position of the (002) diffraction peak via the Bragg's law as $d_{(002)} = \lambda/2\sin\theta$, where λ (0.15451 nm) is the wavelength of Cu-K_α radiation and θ is the Bragg angle [72]. All the calculated $d_{(002)}$-values (0.35–0.39 nm) exceeded that peculiar to crystalline graphite (0.34 nm [73]). Nonetheless, the closest value (0.35 nm) pertained to "the most ordered" sample, GBC(N_2).

As expected [47], the XPS analysis revealed the presence of (12.0–13.7 at.%) potassium in samples BC(N_2), BCG(N_2) and BCG(He) (Fig. S10a). Its relative amount was subtracted to quantify the concentration of the surface oxygen functional species, believed to be beneficial for wettability and pseudocapacitance of the carbonaceous

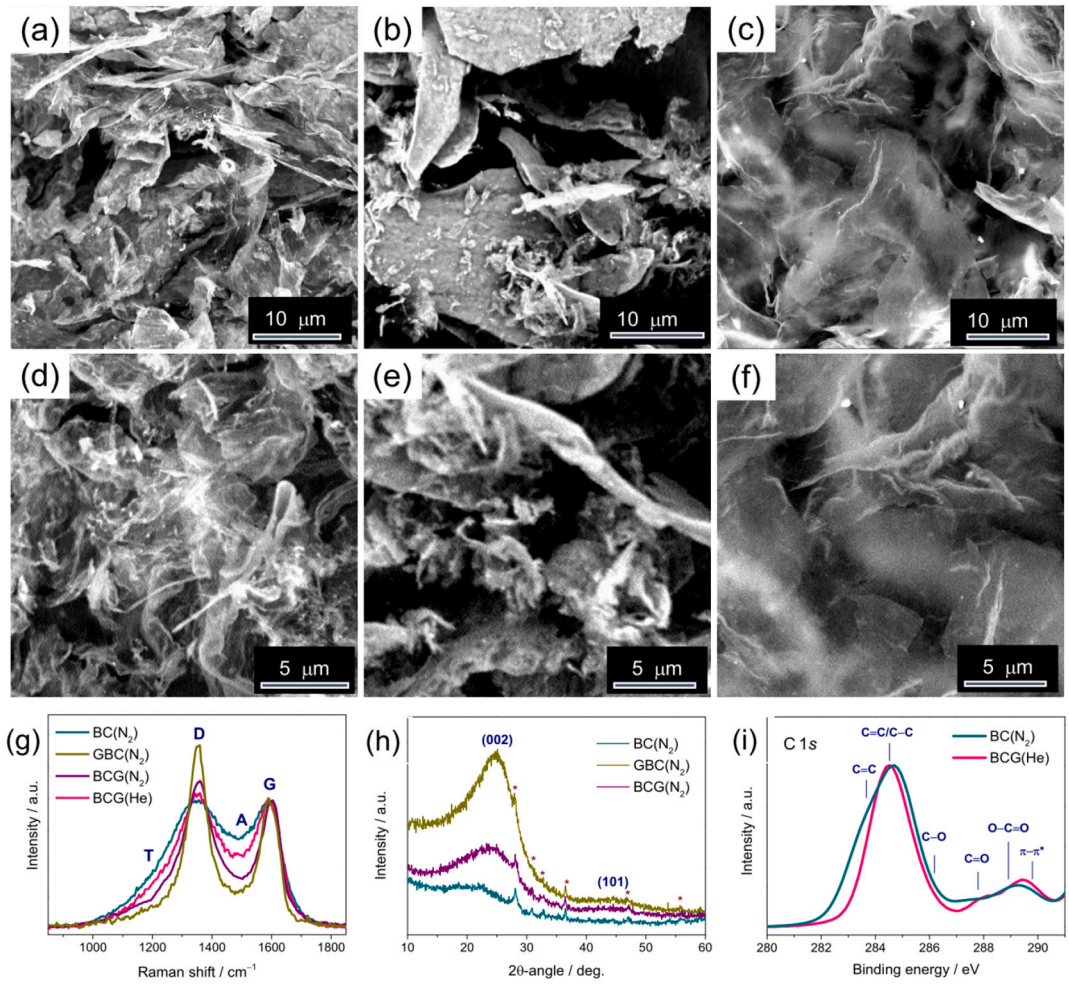

Fig. 2. Results of (a–f) SEM, (g) MRS, (h) XRD and (i) XPS analyses on the processed samples. SEM images refer to samples (a, b, d, e) $BC(N_2)$, and (c, f) $BCG(N_2)$. Micro-Raman spectra are normalised to the G-band maximum intensity for an easier comparison; stars mark spurious peaks originating from the sample-holder in the XRD patterns; high-resolution photoelectron spectra of C 1*s* core level are normalised to the main peak maximum intensity for an easier comparison.

material, as well [50,74,75]. The results obtained by analysing the high-resolution XPS spectra of the samples are reported in Table 2.

In full agreement with the outcomes of MRS and XRD analyses, sample $GBC(N_2)$ exhibits the lowest oxidation degree (O/C atomic ratio: 0.37). The relevant relative amount of oxygenated surface functional species in the remaining samples (40.7–47.1 at.%) accounts for the observed (002) interlayer spacing expansion [72]. It increases in the order $GBC(N_2)$ < $BC(N_2)$ < $BCG(N_2)$ < BCG(He) (Table 2), that is in the same order as the frequency position of the G-band in the micro-Raman spectra (Fig. S11). Thus, although a contribution from C═C chains [68] cannot be ruled out, the band upshift can be thought of as the effect of the electron transfer from the π-states to the oxygen atoms [67,70,76]. The comparison with the data relative to previously studied samples supports this conclusion.

Finally, the greater O/C atomic ratio of BCG(He) compared to $BCG(N_2)$ hints at a higher capability by nitrogen of removing thermally labile oxygenated species, in line with the greater mass loss it produces during the pyrolisation of carbon fibres with respect to helium [77]. A possible explanation for this finding is that, differently from helium, at 700 °C, nitrogen reacts with the oxygenated functional groups present on the material surface with evolution of oxygen containing species (e.g. NO_x species).

In order to get a deeper insight into the oxygenated species present on the sample surface, the high-resolution photoelectron spectra of C 1*s* core level were normalised to the maximum intensity of the main peak and compared (Figs. 2h and S10). Samples BCG(He) (Fig. 2h) and $BCG(N_2)$ (not shown) exhibit similar profiles, with C = C/C–C bonds in aromatic rings (at 284.5 eV), C—O species in hydroxyls (at 286.1 eV), C═O species in carbonyls (at 287.8 eV), O–C = O species in carboxylic groups (at 288.9 eV), and shake-up π–π* satellite (at 289.9 eV) [33,67,78] contributing to the spectral intensity. The C 1*s* profile of sample $BC(N_2)$ further exhibits a shoulder on the lower binding energy side of the main peak. In agreement with the indications inferred from the analysis of micro-Raman spectra, this contribution can be ascribed to *sp*-hybridised C═C species in trans-poly-acetylene-like chains (at 283.6 eV) [79,80]. The relatively high intensity of the shake-up π–π* satellite might be indicative of the presence of localised π–electrons along the polymer chains [81]. Finally, $GBC(N_2)$ exhibits a larger relative amount of C—O species (Fig. S10a) compared to the remaining materials.

3.3. Electrochemical properties of the BC-derived electrode materials

The produced BC-derived nanocarbons were evaluated as active materials for CDI electrodes (Table 3) by carrying out CV measurements in 0.1 M NaCl solutions with potential ranging between −1.3 and 0.4 V and 5–100 mV s^{-1} sweep rates. Fig. S12 compares the CV curves of the investigated electrodes at fixed potential scan rate (ν), whereas Fig. 3 displays the evolution undergone by the curves of each electrode with increasing ν. The measured curves confirm the formation of the electrical double-layer (EDL) for all the electrodes. At fixed ν (100 mV s^{-1}), the CV curve surface area increases in the order BCE-3 < BCE-

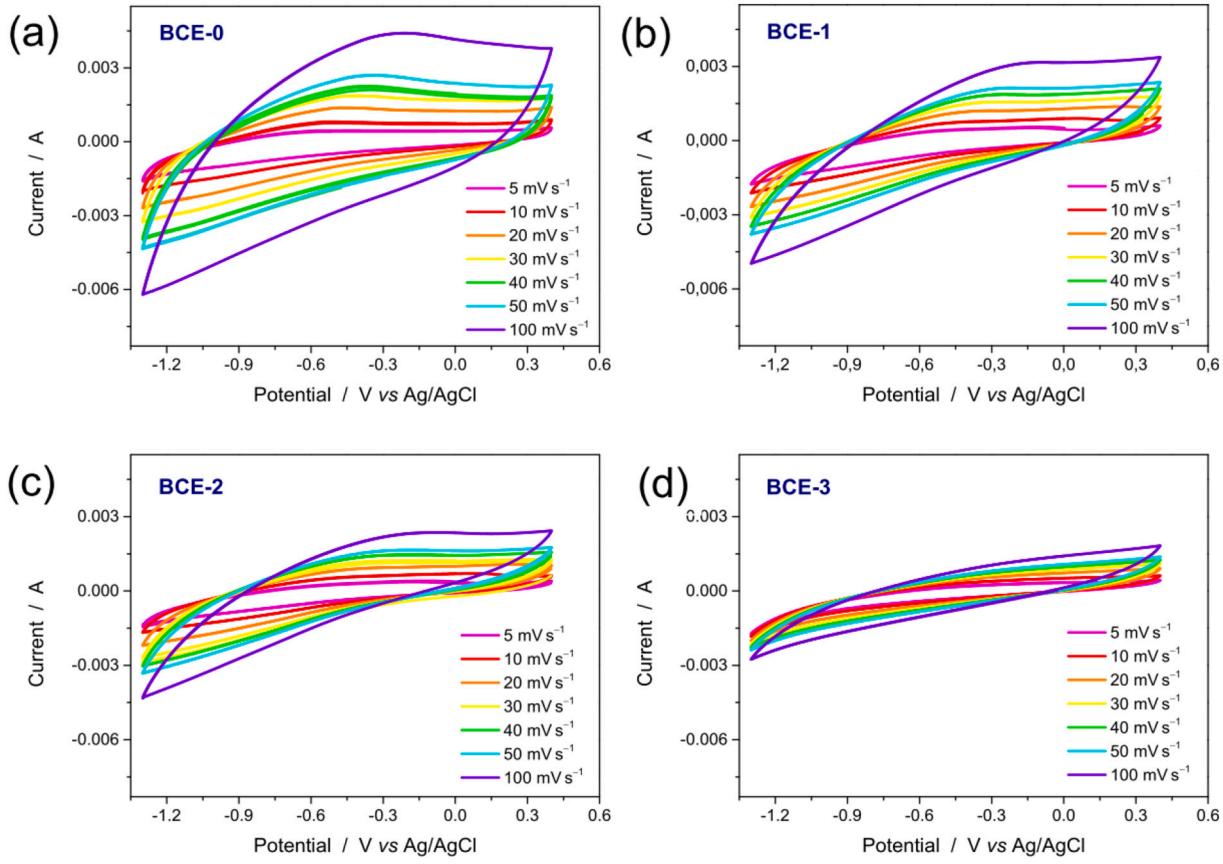

Fig. 3. CV curves of the investigated electrodes.

2 < BCE-1 < BCE-0 (Fig. S12). For a given electrode (Fig. 3), the surface increases with increasing *v*, indicating the progressive reduction of ion transportation rate [82].

In order to more deeply understand the behaviour of the present electrode materials, their electrochemical properties were evaluated also by EIS analysis, a very useful technique to examine capacitive behaviour and internal resistance of the electrode materials [83], by recording the real and imaginary part of the total impedance as a function of the frequency of the input signal. Fig. 4 displays the Nyquist plots obtained from EIS measurements performed, in aqueous 0.1 M NaCl solution, in the $1{\cdot}10^{-1}$-$1{\cdot}10^{4}$ Hz frequency range. For a pure capacitive-behaviour, the Nyquist plot consists of a straight line parallel to the imaginary axis (*y*-axis) in the low frequency region. Each deviation from the ideal behaviour causes the slope of the straight line to diminish and approach 45° in the Nyquist plot. The deviation is ascribed to the increase of Warburg impedance, which is related to the kinetics of the ions diffusion in the solution and to the adsorption of the ions at the electrode/electrolyte interface [37,84,85].

The graphene-enrichment of the active material seems to affect its electrochemical response. The behaviour of (graphene-free) BCE-0 at lower frequencies (Fig. 4a) is the closest to the ideal one among all investigated electrodes, since the Nyquist plot consists of a straight line deviating from the imaginary axis only by 14.6°, which indicates a low Warburg impedance. In the graphene-enriched (GE) active materials, Warburg impedance increases, which points at a non-uniform ions diffusion process at lower frequencies, where the ions movement is partially hindered [86]. In fact, a larger Warburg impedance indicates greater variations in ion diffusion path lengths and increased

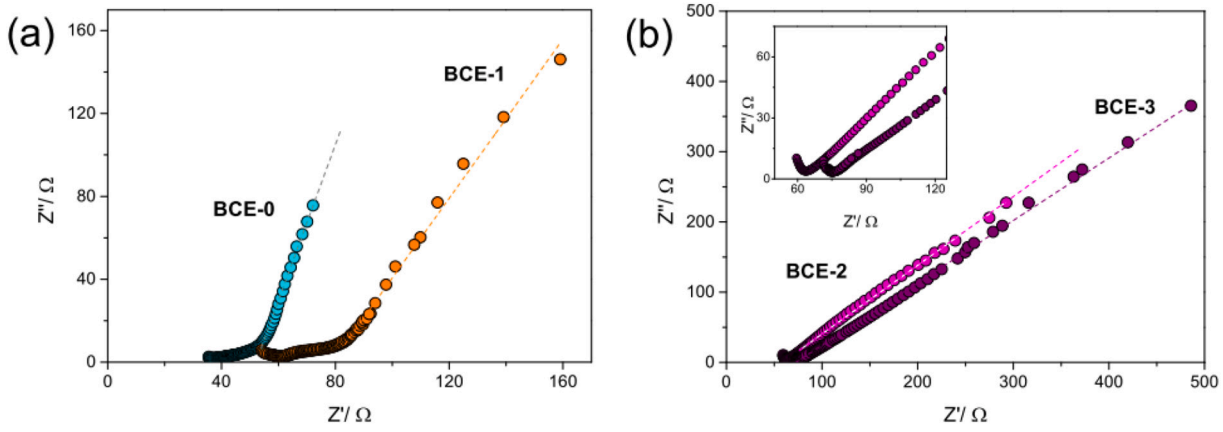

Fig. 4. Nyquist plots of the investigated electrodes (inset: mid-high frequency region of the plots).

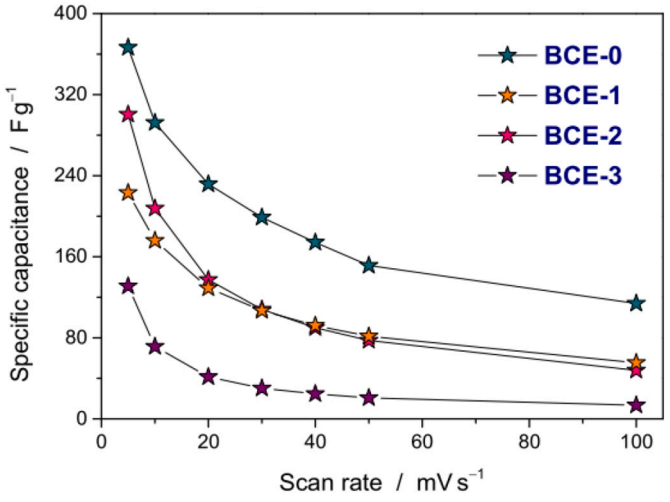

Fig. 5. Specific capacitance of the investigated electrodes as a function of potential scan rate.

obstruction to the ion movement [87]. The increase is in the order BCE-0 < BCE-1 < BCE-2 < BCE-3. The equivalent series resistance (also known as the internal resistance, which includes the bulk electrolyte resistance and the charge transfer resistance), estimated as the intercept of the straight line with the real axis (*x*-axis), increases in the same order, namely BCE-0 (47 Ω) < BCE-1 (60 Ω) < BCE-2 (64 Ω) < BCE-3 (75 Ω).

In the electrode BCE-1, prepared by the use of BC(N_2) + GBC(N_2) physical mixture, the slope changes at 1.5 Hz (Fig. 4a); at lower frequencies, the Nyquist plot consists of a straight line with a slope of 62.5°, whereas in the middle frequency region (from 1.5 Hz to 2 kHz), a semicircle is visible, which indicates the formation of an EDL close to the electrode/electrolyte interface [88]. This behaviour is indicative of the existence of two different charge transfer mechanisms. It originates from the coexistence of two distinct components (namely BC(N_2) and GBC(N_2)) in the hybrid material, as already observed in other physical mixtures [50].

Fig. 5 shows the specific capacitance (C_S) of the electrodes based on the BC-derived nanocarbons, calculated via Eq. (1), as a function of ν. Among the GE electrode materials, the worst performance pertains to BCE-3, which exhibits the lowest capacity at any rate. Besides, the decrease of C_S with the increase of ν from 5 to 100 mV s^{-1}, which gives a qualitative measure of the impact of diffusion as the rate-limiting process [50], is very large (−90.1%). Nonetheless, at 5 mV s^{-1}, its C_S value (131 F g^{-1}) exceeds those measured at the same rate for graphene hydrogel and graphene aerogel electrodes (35 and 18 F g^{-1}, respectively) in an aqueous 1 M NaCl solution [89]; moreover, it equals that reported for commercial carbon powders with very-high surface area at lower rate (2 mV s^{-1}) [90]. These findings suggest that the BC-derived component of the GE-composite provides a beneficial contribution to the overall capacitance. As known [47], upon carbonisation at 700 °C, the dense 3D fibrilar BC skeleton converts into porous carbon with interconnected macropores (> 50 nm), on whose walls mesopores (2–50 nm) and micropores (< 2 nm) develop. The former serve as pathways for efficient ion transport across the electrode, the latter are beneficial to ion storage [82].

Compared to BCE-3, electrode BCE-2 exhibits superior capacity and reduced impact of diffusion as the rate-limiting process (C_S-decrease with ν-increase is −84.0%). As the preparation of the two active materials differs only for the carbonisation atmosphere (He in place of N_2), the larger amount of oxygenated functional moieties present on BCG(He) (Table 2) *partly* justifies the observed improvement, since they contribute to improve both the wettability and pseudocapacitance of the electrode [50,74,75]. The specific capacitance of the hybrid electrode (BCE-1) is comparable to that of BCE-2 for $\nu \geq 20$ mV s^{-1}, whereas below this rate it is smaller. In BCE-1, the impact of ion diffusion as the rate-limiting process further lowers (as ν increases from 5 to 100 mV s^{-1}, C_S diminishes by −75.3%).

BCE-0 outperforms all the GE-electrode materials, even in terms of C_S-diminishing with the scan rate increase (−68.9%). This result is opposite to that previously obtained for electrospun carbon fibres derived from polyacrylonitrile (PAN), which benefited from the graphene-enrichment, in spite of the specific surface area contraction that it caused [11]. The greater C_S-values of electrode BCE-0 with respect to the GE-ones suggest that graphene-enrichment of the active material (regardless of the preparation stage at which it is carried out) fails in improving the material electrochemical performance. A reason for this difference may lie in the experimental procedure for the graphene-enrichment. In the case of electrospun carbon fibres, GO was incorporated into the pristine solution (i.e. *before* the generation of the fibres via electrospinning) [11], which ultimately resulted in an intimate contact between rGO and the PAN-derived carbonaceous fibres and in a homogeneous distribution of it in the fibrous network. On the contrary, in the present case, GO was added onto the surface of the *already synthesised* BC, through immersion or impregnation method (Fig. S2), which resulted in a less uniform distribution of rGO in the bulk of the GE composites and a less intimate contact between it and the BC-derived carbonaceous matrix.

From the comparison with the literature, it emerges that the specific capacitance of electrode BCE-0 at 5 mV s^{-1} (366 F g^{-1}) is greater than that measured by Liu et al. [44], at 2 mV s^{-1} in an aqueous 1 M NaCl solution, for an electrode based on commercial BC carbonised at 800 °C (297 F g^{-1}). The better performance of the present BC-derived nanocarbon might depend on the BC biosynthesis conditions (e.g. bacterial strain, culture medium), as well as on the carbonisation temperature, which is crucial to the pore structure and microstructure of BC-derived carbon materials [47]. Using aqueous 6 M KOH solution as the electrolyte, Zhou et al. [91] obtained a similarly high C_S-value (360 F g^{-1}) for supercapacitors based on porous carbon fibres, produced by block copolymer microphase separation, exhibiting an interconnected network of pores with bimodal distribution, inclusive of *meso*pores (~10 nm) and sub-micropores (~0.5 nm). Ding et al. [47] reported an even larger C_S-value (430 F g^{-1}) for a symmetric supercapacitor using 1 M H_2SO_4 solution as the electrolyte and an ultra-microporous dual-doped carbon, possessing highly concentrated micropores (~ 2 nm) and a considerable amount of sub-micropores (< 1 nm), as the active material. Sub-micropores, which significantly enhanced the capacitive performance due to pore confinement effect [47], resulted from the simultaneous activation/carbonisation of the dense BC precursor, with potassium hydroxide acting as the activating agent.

In sample BC(N_2), the analysis of the nitrogen adsorption/desorption isotherms evidenced the presence of sub-micropores with size < 0.5 nm, as reported by Ding et al. [47]. The specific micro-pore volume was 0.206 cm^3 g^{-1}; the specific surface area was 340 m^2 g^{-1}. Although comparable with those reported for other BC-derived nanocarbons [44], the latter value could be underestimated [92]. In the composites only a slight increase of the pore size and a slight reduction of specific surface area were observed, in full agreement with what previously observed in electrospun carbon fibres [11] and with the results reported in the literature, as well [93].

Outstanding storage and desalination properties have recently been reported for carbons simultaneously having a hierarchically porous structure consisting of interconnected macro-/meso-/micro-pores and high (intrinsic and heteroatom-induced) defect density [94,95]. Besides, the predominant influence of the carbon defects, with respect to the functional groups, on capacitance has been pointed out [96]. As a matter of fact, BC(N_2) possesses the hierarchical porosity peculiar to BC-derived carbons and, besides, the highest amorphousness degree, with a plethora of different morphological defects (Fig. S9) and the largest fraction of the highly reactive [70] non-sp^2 defects, including

Csp^3 species interconnecting the graphitic domains and chains with localised states at the edge-sites. The synergy between these active sites and the material porosity accounts for its remarkable electrochemical performance [97].

3.4. Correlations between electrochemical properties and defectiveness of the electrode materials

In the last decades, increasing the graphitisation degree and decreasing the defect density (e.g. by enhancing the carbonisation temperature) has represented the most common strategy to improve the electrochemical performance of carbon-based materials. Very recently, in counter-tendency, several authors have pointed out the crucial role of defects in ion storage and emphasised the benefits deriving from producing defect-rich nanocarbons [92–95,97–100]. Just to cite a few of cases, Guo et al. [99] have reported that hard carbon nanofibres with a defect-richer texture exhibit better rate capability and noticeably longer cycle performance. Yao et al. [97] have shown that defects at the graphene layer edges in microporous soft carbons provide extra sodium-ion storage sites. Lu et al. [100] have attributed to the higher defect concentration the enhanced Na storage performance of soft carbon prepared at lower carbonisation temperature. Novel models involving Na-ion storage at defect sites, rather than intercalation between graphene sheets, have been further proposed to explain the sodiation process in non-graphitisable carbons [98].

In the present case, the increase of the specific capacitance moving from the least defective electrode material (BCE-3) to the defect-richest one (BCE-0) proves that the carbon defect sites play a crucial role in the ion adsorption process, in line with the most recent assessments on their ability to generate more accessible surface area, favouring the charge accumulation [44].

It can be envisaged that, at low scan rates, time for the ions of the electrolyte is enough to diffuse into the inner pores of the electrodes [50], where they are adsorbed at the defect-sites, regardless of their type. Actually, a good correlation is found by plotting the specific capacitance at 5 mV s^{-1} scan rate (Fig. 6a) against the relative intensity of all the Raman "defect-bands" $(I_T + I_D + I_A)/I_G$. This indicates that all types of defects contribute to the ion adsorption and to the formation of EDL at the lowest potential scan rate. The non-linearity of the found relationship might reflect the different chemical reactivity of the various type of defects [68,70,101,102]. With increasing scan rate, the diffusion becomes rate-limiting [103] and the moving ions do not have time enough to accumulate onto the less accessible surface regions, which are progressively excluded [50]. Under these conditions, the ion adsorption takes place preferentially at the most reactive non-sp^2 sites on the pore surface, e.g. single vacancies and dandling bonds at zig-zag edges [101,102]. Actually, the specific capacitance at 100 mV s^{-1} scan rate (Fig. 6b) linearly correlates with the intensity ratio, $(I_T + I_A)/I_D$, of the bands originating from non-sp^2 and sp^2 defects. The increase in the density of the non-sp^2 defects with respect to sp^2 ones is able to account also for the decrease in internal resistance from electrode BCE-3 to BCE-0 (Fig. S13a), as well as for the variation of C_s with the increase of ν. Ion diffusion has lighter impact as the rate-limiting process (i.e. less negative value of the C_s-variation) in materials with a larger relative amount of non-sp^2 defects, in line with the outcomes of computational studies on the reactivity of carbon defects with sodium ions [104].

Remarkably, the data relative to the electrodes based on PAN-derived carbon fibres previously investigated [11] show the same trend (Fig. S13), even if, obviously, they cannot line-up along the curves of BC-derived nanocarbons owing the large differences in the other influential factors (e.g. specific surface area, concentration and type of surface functional species).

3.5. Electrosorptive properties of the BC-derived electrode materials

Typically, materials possessing superior capacitive performance exhibit enhanced electrosorptive properties. Fig. 7a displays the salt adsorption capacity, *SAC*, of the electrodes BCE-0, BCE-1 and BCE-2, as calculated via Eq. (2), at various NaCl concentrations. As a general trend, as the concentration increases, the amount of NaCl removed from the solution raises as a result of the enhanced mass transfer rate of ions inside the micropores and of the reduced EDL thickness and overlapping effects [11,105,106]. In the present case, the increase of salt concentration from 585 mg L^{-1} (10 mmol L^{-1}) to 11.7 g L^{-1} (200 mmol L^{-1}) causes *SAC*-values to increase from 60.7 mg g^{-1} to 1.35 g g^{-1} for electrode BCE-0, from 55.0 mg g^{-1} to 1.03 g g^{-1} for electrode BCE-1 and from 79.0 mg g^{-1} to 1.11 g g^{-1} for electrode BCE-2. The comparison with the literature (Table 4) clearly proves that these represent unprecedented electrosorption capacities for carbon-based electrodes. At 585 mg L^{-1} and 1.2 V, present electrode materials are able to remove a greater amount of salt (55.0–79.0 mg g^{-1}) compared to that removed at the same concentration and applied voltage by PAN-derived C fibres (13.7–26.8 mg g^{-1}), and at 500 mg L^{-1} and 2.0 V by graphene aerogel and graphene hydrogel (45.9–49.3 mg g^{-1}). At the initial concentration of 58.5 mg L^{-1} (1 mmol L^{-1}), the amount of NaCl adsorbed on electrode BCE-0 (8.3 mg g^{-1}) is nearly twice that adsorbed on CNT sponge at comparable concentration (4.3 mg g^{-1}). The smaller specific surface area of PAN-derived C fibres, graphene aerogel and CNT sponge might be responsible for their lower *SAC*-values.

Interestingly, below 5.85 g L^{-1}, *SAC* increases in the order BCE-1 < BCE-0 < BCE-2. This strongly points at the crucial role of the electrode wettability at lower solute concentrations. Actually, a linear correlation (Fig. 7b) is found between *SAC*-values at 585 mg L^{-1} (10 mmol L^{-1}) and the concentration of surface functional species (Table 2), which, as known [11,50,74,75], improve the wettability of the carbonaceous electrode by the electrolyte and their pseudocapacitance. In the presence of lower mass transfer rate of ions and higher EDL thickness and overlapping effects, the wettability/accessibility of the electrode surface and pseudocapacitive reactions become relevant factors for the ion adsorption.

At 5.85 g L^{-1} (100 mmol L^{-1}), the electrosorptive performance of electrodes BCE-0 and BCE-2 is reversed, with *SAC* of BCE-0 exceeding that of BCE-2. This suggests that, at higher salt concentrations, the defectiveness of the active material becomes the most influential property, as it controls the relative amount of active sites available for the electrostatic adsorption. *SAC*-values at 5.85 g L^{-1} well correlate with non-sp^2 to sp^2 defect density ratio (Fig. 7c). Despite the large differences in the manifold factors involved in the process, the data relative to the electrodes based on PAN-derived carbon fibres [11], show the same trend (Fig. S14), thus supporting these conclusions.

4. Conclusions

BC is utilised as a carbon precursor for the preparation of electrode materials for the CDI of water, which exhibit unprecedented desalination capacities for nanocarbons (55–79 mg g^{-1} of salt at an initial concentration of 585 mg L^{-1}).

The thorough investigation of the physico-chemical and electrochemical properties of the materials produced allows drawing the following conclusions:

- The BC-derived nanocarbons exhibit a three-dimensional architecture featured by hierarchical porosity, different density and type of lattice defects and high content of surface oxygen species (45–54 wt%).
- The carbon network defectiveness strongly affects the electro-chemical behaviour of the electrodes, whose specific capacitance increases with the defect density. All types of lattice defects participate in ion storage at lower scan rates. As the scan rate increases, the diffusion becomes rate limiting and the ions, having not time enough to move, accumulate preferentially at the most reactive non-sp^2 sites on the pore surface.

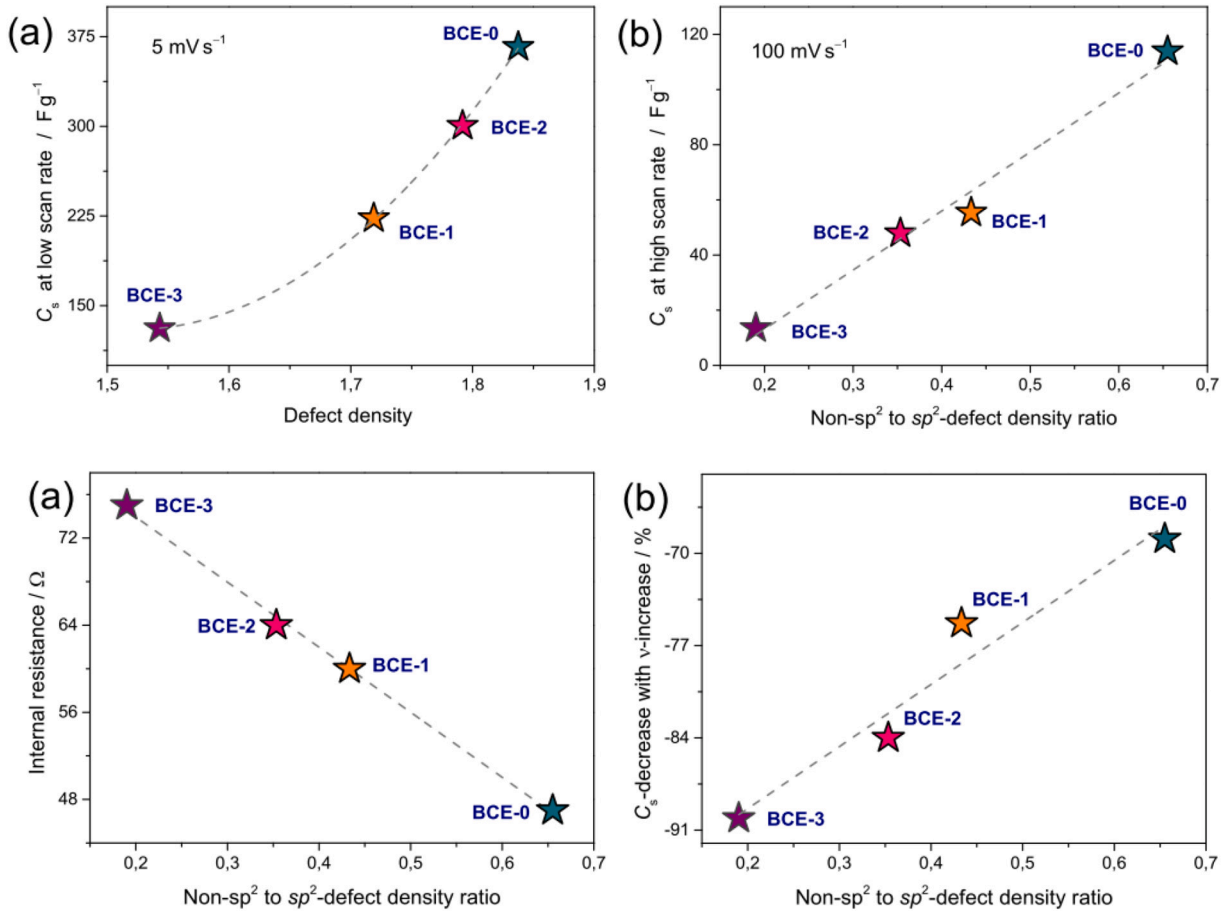

Fig. 6. Correlation between quantities describing the electrochemical behaviour of the investigated electrodes and the density of defect-sites, as depicted by the intensities of the Raman T-, A- and D-bands.

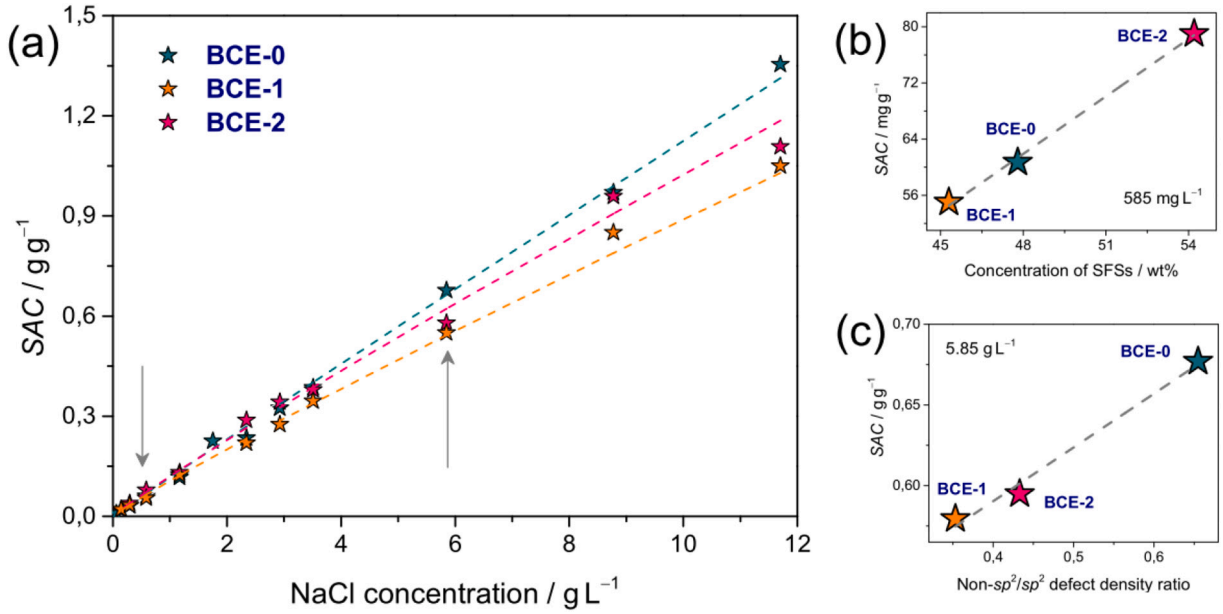

Fig. 7. (a) Salt adsorption capacity (*SAC*), of the investigated; the best fits of the data (dashed lines) to the Freundlich adsorption isotherms are also shown. *SAC* values at (b) 585 mg L^{-1} and (c) 5.85 g L^{-1} NaCl concentrations as a function of the concentration of surface functional species (SFSs) and non-sp^2 to sp^2 defect density ratio, respectively.

Table 4
NaCl adsorption capacities of various CDI electrodes based on different carbon nanomaterials. C_0 indicates the initial salt concentration; *SSA* stands for specific surface area.

Active electrode material	C_0/mg L^{-1}	Voltage/V	*SSA*/m^2 g^{-1}	*SAC*/mg g^{-1}	Ref.
Graphene	780	2.0	362	22.3	[107]
SWCNTs/Graphene	780	2.0	391	26.4	[107]
3D Graphene	572	2.0	124	29.6	[108]
Graphene aerogel	500	2.0	193	45.9	[89]
Graphene hydrogel	500	2.0	517	49.3	[89]
3DNGR(an.)/3DSGR (cath.)	500	1.4		13.7	[109]
N,P-doped HPCN-900	250	1.4	1679	18.1	[95]
3D porous G hydrogel	5000	1.2		26.8	[110]
BC-derived CNF800	1000	1.2	585	12.8	[111]
BC-derived N-doped CNF800	1000	1.2	785	17.3	[111]
N-doped C fibres	585	1.2	20	17.0	[11]
GE N-doped C fibres	585	1.2	17	27.6	[11]
BCE-1	585	1.2		55.0	This work
BCE-2	585	1.2		79.0	This work
BCE-0	585	1.2	340	60.7	This work
BC-derived CNF800	500	1.2	586	10.7	[44]
N,P-doped HPCN-900	250	1.2	1679	10.3	[95]
BCE-1	146	1.2		21.0	This work
BCE-2	146	1.2		18.6	This work
BCE-0	146	1.2	340	18.9	This work
Nanoporous C polyhedra	100	1.2	785	9.4	[112]
AC	100	1.2	1654	13.2	[112]
Activ. nanop. C polyhedra	100	1.2	2474	24.4	[112]
RGO/ACF-10	95	1.2	621	7.2	[113]
CNT sponge	60	1.2	60–80	4.3	[114]
BCE-0	58.5	1.2	340	8.3	This work

- The relative amount of oxygenated species on the electrode surface enhancing its wettability play a crucial role in the salt adsorption capacity at lower concentrations. At higher NaCl concentrations, the availability of active non-sp^2 defect sites for adsorption becomes the key-factor.

The above conclusions still hold for the previously investigated electrospun carbon fibres and are perfectly in line with the most recent literature reports focused on defect-rich nanocarbons and the fundamental role of defects in ion storage.

Author contributions

Y.B. did the electrochemical tests and porosimetry measurements, F.P. performed the thermal treatments, SEM/EDX, TGA and XRD measurements, L.U., M.A.C. and A.E. took care of the BC biosynthesis, A.P. performed the XPS measurements, C.T. conducted the Raman measurements and contributed to the data analysis, S.S. analysed the data, conceived, designed, and wrote the manuscript. All authors discussed the results and commented the manuscript.

Declaration of competing interest

The authors declare that they have no known competing financial interests or personal relationships that could have appeared to influence the work reported in this paper.

Acknowledgment

L.U., M.A.C. and A.E. gratefully thank GIU18/216-UPV/EHU Research Group for the financial support to their work.

Appendix A. Supplementary data

Supplementary data to this article can be found online at https://doi.org/10.1016/j.desal.2020.114596.

References

[1] United Nations, https://www.unwater.org/water-facts/scarcity/.
[2] United Nations, https://www.un.org/waterforlifedecade/scarcity.shtml.
[3] M. Elimelech, W.A. Phillip, The future of seawater desalination: energy, technology, and the environment, Science 333 (2011) 712–717, https://doi.org/10.1126/science.1200488.
[4] Y. Oren, Capacitive deionization (CDI) for desalination and water treatment - past, present and future (a review), Desalination. 228 (2008) 10–29, https://doi.org/10.1016/J.DESAL.2007.08.005.
[5] S. Porada, R. Zhao, A. van der Wal, V. Presser, P.M. Biesheuvel, Review on the science and technology of water desalination by capacitive deionization, Prog. Mater. Sci. 58 (2013) 1388–1442, https://doi.org/10.1016/J.PMATSCI.2013.03.005.
[6] A. Kalfa, B. Shapira, A. Shopin, I. Cohen, E. Avraham, D. Aurbach, Capacitive deionization for wastewater treatment: opportunities and challenges, Chemosphere. 241 (2020) 125003, https://doi.org/10.1016/J.CHEMOSPHERE.2019.125003.
[7] M.A. Luciano, H. Ribeiro, G.E. Bruch, G.G. Silva, Efficiency of capacitive deionization using carbon materials based electrodes for water desalination, J. Electroanal. Chem. 859 (2020) 113840, https://doi.org/10.1016/J.JELECHEM.2020.113840.
[8] H. Yin, S. Zhao, J. Wan, H. Tang, L. Chang, L. He, H. Zhao, Y. Gao, Z. Tang, Three-dimensional graphene/metal oxide nanoparticle hybrids for high-performance capacitive deionization of saline water, Adv. Mater. 25 (2013) 6270–6276, https://doi.org/10.1002/adma.201302223.
[9] Z.H. Huang, Z. Yang, F. Kang, M. Inagaki, Carbon electrodes for capacitive deionization, J. Mater. Chem. A 5 (2017) 470–496, https://doi.org/10.1039/C6TA06733F.
[10] B. Jia, W. Zhang, Preparation and application of electrodes in capacitive deionization (CDI): a state-of-art review, Nanoscale Res. Lett. 11 (2016) 64, https://doi.org/10.1186/s11671-016-1284-1.
[11] Y. Belaustegui, S. Zorita, F. Fernández-Carretero, A. García-Luis, F. Pantò, S. Stelitano, P. Frontera, P. Antonucci, S. Santangelo, Electro-spun graphene-enriched carbon fibres with high nitrogen-contents for electrochemical water desalination, Desalination. 428 (2018) 40–49, https://doi.org/10.1016/J.DESAL.2017.11.019.
[12] C. Castro, I. Cleenwerck, R. Zuluaga, G. Caro, J.-L. Putaux, O.J. Rojas, P. Gañán, Production of bacterial cellulose: Use of a new strain of microorganism, Handb. Green Mater. WORLD SCIENTIFIC, 2013, pp. 105–122, , https://doi.org/10.1142/9789814566469_0008.
[13] G.F. Perotti, H.S. Barud, S.J.L. Ribeiro, V.R.L. Constantino, Bacterial cellulose as a template for preparation of hydrotalcite-like compounds, J. Braz. Chem. Soc. 25 (2014) 1647–1655, https://doi.org/10.5935/0103-5053.20140153.
[14] R. Shah, R. Vyroubal, H. Fei, N. Saha, T. Kitano, P. Saha, Preparation of Bacterial Cellulose Based Hydrogels and Their Viscoelastic Behavior, (2015), p. 040007, https://doi.org/10.1063/1.4918895.
[15] S.S. Wang, Y.H. Han, Y.X. Ye, X.X. Shi, P. Xiang, D.L. Chen, M. Li, Physicochemical characterization of high-quality bacterial cellulose produced by Komagataeibacter sp. strain W1 and identification of the associated genes in bacterial cellulose production, RSC Adv. 7 (2017) 45145–45155 https://doi.org/10.1039/C7RA08391B.
[16] E. Tsouko, C. Kourmentza, D. Ladakis, N. Kopsahelis, I. Mandala, S. Papanikolaou, F. Paloukis, V. Alves, A. Koutinas, Bacterial cellulose production from industrial waste and by-product streams, Int. J. Mol. Sci. 16 (2015) 14832–14849, https://doi.org/10.3390/ijms160714832.
[17] M. Szymańska-Chargot, J. Cybulska, A. Zdunek, Sensing the structural differences in cellulose from apple and bacterial cell wall materials by Raman and FT-IR spectroscopy, Sensors. 11 (2011) 5543–5560, https://doi.org/10.3390/s110605543.
[18] E. Erbas Kiziltas, A. Kiziltas, K. Rhodes, N.W. Emanetoglu, M. Blumentritt, D.J. Gardner, Electrically conductive nano graphite-filled bacterial cellulose composites, Carbohydr. Polym. 136 (2016) 1144–1151, https://doi.org/10.1016/J.CARBPOL.2015.10.004.
[19] A.M. Hernández-Arriaga, C. del Cerro, L. Urbina, A. Eceiza, M.A. Corcuera, A. Retegi, M. Auxiliadora Prieto, Genome sequence and characterization of the bcs clusters for the production of nanocellulose from the low pH resistant strain Komagataeibacter medellinensis ID13488, Microb. Biotechnol. 12 (2019) 620–632, https://doi.org/10.1111/1751-7915.13376.
[20] M. Moniri, A. Boroumand Moghaddam, S. Azizi, R. Abdul Rahim, A. Bin Ariff, W. Zuhainis Saad, M. Navaderi, R. Mohamad, Production and status of bacterial cellulose in biomedical engineering, Nanomaterials 7 (2017) 257, https://doi.org/10.3390/nano7090257.
[21] G.F. Picheth, C.L. Pirich, M.R. Sierakowski, M.A. Woehl, C.N. Sakakibara, C.F. de Souza, A.A. Martin, R. da Silva, R.A. de Freitas, Bacterial cellulose in biomedical applications: a review, Int. J. Biol. Macromol. 104 (2017) 97–106, https://doi.org/

10.1016/J.IJBIOMAC.2017.05.171.
[22] L. Urbina, A. Alonso-Varona, A. Saralegi, T. Palomares, A. Eceiza, M.Á. Corcuera, A. Retegi, Hybrid and biocompatible cellulose/polyurethane nanocomposites with water-activated shape memory properties, Carbohydr. Polym. 216 (2019) 86–96, https://doi.org/10.1016/J.CARBPOL.2019.04.010.
[23] N. Halib, I. Ahmad, M. Grassi, G. Grassi, The remarkable three-dimensional network structure of bacterial cellulose for tissue engineering applications, Int. J. Pharm. 566 (2019) 631–640, https://doi.org/10.1016/J.IJPHARM.2019.06.017.
[24] P. Weyell, U. Beekmann, C. Küpper, M. Dederichs, J. Thamm, D. Fischer, D. Kralisch, Tailor-made material characteristics of bacterial cellulose for drug delivery applications in dentistry, Carbohydr. Polym. 207 (2019) 1–10, https://doi.org/10.1016/J.CARBPOL.2018.11.061.
[25] P. Pourali, N. Razavianzadeh, L. Khojasteh, B. Yahyaei, Assessment of the cutaneous wound healing efficiency of acidic, neutral and alkaline bacterial cellulose membrane in rat, J. Mater. Sci. Mater. Med. 29 (2018) 90, https://doi.org/10.1007/s10856-018-6099-4.
[26] L. Urbina, A. Eceiza, N. Gabilondo, M.Á. Corcuera, A. Retegi, Valorization of apple waste for active packaging: multicomponent polyhydroxyalkanoate coated nanopapers with improved hydrophobicity and antioxidant capacity, Food Packag. Shelf Life 21 (2019) 100356, https://doi.org/10.1016/J.FPSL.2019.100356.
[27] H.M.C. Azeredo, H. Barud, C.S. Farinas, V.M. Vasconcellos, A.M. Claro, Bacterial cellulose as a raw material for food and food packaging applications, Front. Sustain. Food Syst. 3 (2019) 7 https://www.frontiersin.org/article/10.3389/fsufs.2019.00007.
[28] L. Urbina, O. Guaresti, J. Requies, N. Gabilondo, A. Eceiza, M.A. Corcuera, A. Retegi, Design of reusable novel membranes based on bacterial cellulose and chitosan for the filtration of copper in wastewaters, Carbohydr. Polym. 193 (2018) 362–372, https://doi.org/10.1016/J.CARBPOL.2018.04.007.
[29] J.T. McNamara, J.L.W. Morgan, J. Zimmer, A molecular description of cellulose biosynthesis, Annu. Rev. Biochem. 84 (2015) 895–921, https://doi.org/10.1146/annurev-biochem-060614-033930.
[30] M.L. Foresti, A. Vázquez, B. Boury, Applications of bacterial cellulose as precursor of carbon and composites with metal oxide, metal sulfide and metal nanoparticles: a review of recent advances, Carbohydr. Polym. 157 (2017) 447–467, https://doi.org/10.1016/J.CARBPOL.2016.09.008.
[31] K.Y. Lee, H. Qian, F.H. Tay, J.J. Blaker, S.G. Kazarian, A. Bismarck, Bacterial cellulose as source for activated nanosized carbon for electric double layer capacitors, J. Mater. Sci. 48 (2013) 367–376, https://doi.org/10.1007/s10853-012-6754-y.
[32] W. Ouyang, J. Sun, J. Memon, C. Wang, J. Geng, Y. Huang, Scalable preparation of three-dimensional porous structures of reduced graphene oxide/cellulose composites and their application in supercapacitors, Carbon N. Y. 62 (2013) 501–509, https://doi.org/10.1016/J.CARBON.2013.06.049.
[33] V. Kuzmenko, N. Wang, M. Haque, O. Naboka, M. Flygare, K. Svensson, P. Gatenholm, J. Liu, P. Enoksson, Cellulose-derived carbon nanofibers/graphene composite electrodes for powerful compact supercapacitors, RSC Adv. 7 (2017) 45968–45977, https://doi.org/10.1039/C7RA07533B.
[34] D.C. Wang, H.Y. Yu, D. Qi, M. Ramasamy, J. Yao, F. Tang, K. (Michael) C. Tam, Q. Ni, Supramolecular self-assembly of 3D conductive cellulose nanofiber aerogels for flexible supercapacitors and ultrasensitive sensors, ACS Appl. Mater. Interfaces 11 (2019) 24435–24446, https://doi.org/10.1021/acsami.9b06527.
[35] Z. Gui, H. Zhu, E. Gillette, X. Han, G.W. Rubloff, L. Hu, S.B. Lee, Natural cellulose fiber as substrate for supercapacitor, ACS Nano 7 (2013) 6037–6046, https://doi.org/10.1021/nn401818t.
[36] J.M. Zhang, Q. Hua, J. Li, J. Yuan, T. Peijs, Z. Dai, Y. Zhang, Z. Zheng, L. Zheng, J. Tang, Cellulose-derived highly porous three-dimensional activated carbons for supercapacitors, ACS Omega 3 (2018) 14933–14941, https://doi.org/10.1021/acsomega.8b02075.
[37] Y. Zhang, Z. Shang, M. Shen, S.P. Chowdhury, A. Ignaszak, S. Sun, Y. Ni, Cellulose nanofibers/deduced graphene oxide/polypyrrole aerogel electrodes for high-capacitance flexible all-solid-state supercapacitors, ACS Sustain. Chem. Eng. 7 (2019) 11175–11185, https://doi.org/10.1021/acssuschemeng.9b00321.
[38] J. Virtanen, A. Pammo, J. Keskinen, E. Sarlin, S. Tuukkanen, Pyrolysed cellulose nanofibrils and dandelion pappus in supercapacitor application, Cellulose. 24 (2017) 3387–3397, https://doi.org/10.1007/s10570-017-1332-8.
[39] P. Song, X. Shen, X. He, K. Feng, L. Kong, Z. Ji, L. Zhai, G. Zhu, D. Zhang, Cellulose-derived nitrogen-doped hierarchically porous carbon for high-performance supercapacitors, Cellulose. 26 (2019) 1195–1208, https://doi.org/10.1007/s10570-018-2115-6.
[40] B.M. Lee, J.J. Eom, G.Y. Baek, S.-K. Hong, J.P. Jeun, J.H. Choi, J.M. Yun, Cellulose non-woven fabric-derived porous carbon films as binder-free electrodes for supercapacitors, Cellulose. 26 (2019) 4529–4540, https://doi.org/10.1007/s10570-019-02380-6.
[41] M.P. Illa, M. Khandelwal, C.S. Sharma, Bacterial cellulose-derived carbon nanofibers as anode for lithium-ion batteries, Emergent Mater. 1 (2018) 105–120, https://doi.org/10.1007/s42247-018-0012-2.
[42] B. Wang, X. Li, B. Luo, J. Yang, X. Wang, Q. Song, S. Chen, L. Zhi, Pyrolyzed bacterial cellulose: a versatile support for lithium ion battery anode materials, Small. 9 (2013) 2399–2404, https://doi.org/10.1002/smll.201300692.
[43] Y. Huang, Z. Lin, M. Zheng, T. Wang, J. Yang, F. Yuan, X. Lu, L. Liu, D. Sun, Amorphous Fe_2O_3 nanoshells coated on carbonized bacterial cellulose nanofibers as a flexible anode for high-performance lithium ion batteries, J. Power Sources 307 (2016) 649–656, https://doi.org/10.1016/J.JPOWSOUR.2016.01.026.
[44] Y. Liu, T. Lu, Z. Sun, D.H.C. Chua, L. Pan, Ultra-thin carbon nanofiber networks derived from bacterial cellulose for capacitive deionization, J. Mater. Chem. A 3 (2015) 8693–8700, https://doi.org/10.1039/C5TA00435G.
[45] Y. Wan, F. Zhang, C. Li, G. Xiong, Y. Zhu, H. Luo, Facile and scalable production of three-dimensional spherical carbonized bacterial cellulose/graphene nanocomposites with a honeycomb-like surface pattern as potential superior absorbents, J. Mater. Chem. A 3 (2015) 24389–24396, https://doi.org/10.1039/C5TA07464A.
[46] B. Dai, Y. Ren, G. Wang, Y. Ma, P. Zhu, S. Li, Microstructure and dielectric properties of biocarbon nanofiber composites, Nanoscale Res. Lett. 8 (2013) 293, https://doi.org/10.1186/1556-276X-8-293.
[47] C. Ding, T. Liu, X. Yan, L. Huang, S. Ryu, J. Lan, Y. Yu, W.H. Zhong, X. Yang, An ultra-microporous carbon material boosting integrated capacitance for cellulose-based supercapacitors, Nano-Micro Lett. 12 (2020) 63, https://doi.org/10.1007/s40820-020-0393-7.
[48] K. Barbera, L. Frusteri, G. Italiano, L. Spadaro, F. Frusteri, S. Perathoner, G. Centi, Low-temperature graphitization of amorphous carbon nanospheres, Chinese J. Catal. 35 (2014) 869–876, https://doi.org/10.1016/S1872-2067(14)60098-X.
[49] J.F. Moulder, W.F. Stickle, P.E. Sobol, K.D. Bomben, J. Chastain (Ed.), Handbook of X-ray Photoelectron Spectroscopy, 118 Perkin-Elmer, Eden Prairie, MN, 1992edited by. 1992.
[50] S. Santangelo, F. Pantò, C. Triolo, S. Stelitano, P. Frontera, F. Fernández-Carretero, I. Rincon, P. Azpiroz, A. García-Luis, Y. Belaustegui, Evaluation of the electrochemical performance of electrospun transition metal oxide-based electrode nanomaterials for water CDI applications, Electrochim. Acta 309 (2019) 125–139, https://doi.org/10.1016/j.electacta.2019.04.075.
[51] M.E. Suss, S. Porada, X. Sun, P.M. Biesheuvel, J. Yoon, V. Presser, Water desalination via capacitive deionization: what is it and what can we expect from it? Energy Environ. Sci. 8 (2015) 2296–2319, https://doi.org/10.1039/C5EE00519A.
[52] W.K. Czaja, D.J. Young, M. Kawecki, R.M. Brown, The future prospects of microbial cellulose in biomedical applications, Biomacromolecules. 8 (2007) 1–12, https://doi.org/10.1021/bm060620d.
[53] L. Urbina, A.M. Hernández-Arriaga, A. Eceiza, N. Gabilondo, M.A. Corcuera, M.A. Prieto, A. Retegi, By-products of the cider production: an alternative source of nutrients to produce bacterial cellulose, Cellulose. 24 (2017) 2071–2082, https://doi.org/10.1007/s10570-017-1263-4.
[54] L. Segal, J.J. Creely, A.E. Martin, C.M. Conrad, An empirical method for estimating the degree of crystallinity of native cellulose using the X-ray diffractometer, Text. Res. J. 29 (1959) 786–794, https://doi.org/10.1177/004051755902901003.
[55] D.V. Parikh, D.P. Thibodeaux, B. Condon, X-ray crystallinity of bleached and crosslinked cottons, Text. Res. J. 77 (2007) 612–616, https://doi.org/10.1177/0040517507081982.
[56] P.K. Kulkarni, S.A. Dixit, U.B. Singh, Evaluation of bacterial cellulose produced form Acetobacter xylinum as pharmaceutical excipient, Am. J. Drug Discovery Dev. 2 (2012) 72–86, https://doi.org/10.3923/ajdd.2012.72.86.
[57] A.P.P. Alves, L.P. de Oliveira, A.A. Castro, R. Neumann, L.F. de Oliveira, H.G. Edwards, A.C. Sant'Ana, The structure of different cellulosic fibres characterized by Raman spectroscopy, Vib. Spectrosc. 86 (2016) 324–330, https://doi.org/10.1016/j.vibspec.2016.08.007.
[58] U.P. Agarwal, R.S. Reiner, S.A. Ralph, Cellulose I crystallinity determination using FT–Raman spectroscopy: univariate and multivariate methods, Cellulose 17 (2010) 721–733, https://doi.org/10.1007/s10570-010-9420-z.
[59] U.P. Agarwal, Raman spectroscopy in the analysis of cellulose nanomaterials, Nanocelluloses: Their Preparation, Properties, and Applications, American Chemical Society, ACS Symposium Series, 2017, pp. 75–90, , https://doi.org/10.1021/bk-2017-1251.ch004 Washington.
[60] H. Si, H. Luo, G. Xiong, Z. Yang, S.R. Raman, R. Guo, Y. Wan, One-step in situ biosynthesis of graphene oxide–bacterial cellulose nanocomposite hydrogels, Macromol. Rapid Commun. 35 (2014) 1706–1711, https://doi.org/10.1002/marc.201400239.
[61] H. Luo, G. Xiong, Z. Yang, S.R. Raman, H. Si, Y. Wan, A novel three-dimensional graphene/bacterial cellulose nanocomposite prepared by in situ biosynthesis, RSC Adv. 4 (2014) 14369–14372, https://doi.org/10.1039/C4RA00318G.
[62] H. Luo, H. Ao, M. Peng, F. Yao, Z. Yang, Y. Wan, Effect of highly dispersed graphene and graphene oxide in 3D nanofibrous bacterial cellulose scaffold on cell responses: a comparative study, Mater. Chem. Phys. 235 (2019) 121774, https://doi.org/10.1016/j.matchemphys.2019.121774.
[63] W. Zhu, W. Li, Y. He, T. Duan, In-situ biopreparation of biocompatible bacterial cellulose/graphene oxide composites pellets, Appl. Surf. Sci. 338 (2015) 22–26, https://doi.org/10.1016/j.apsusc.2015.02.030.
[64] A.C. Ferrari, J. Robertson, Interpretation of Raman spectra of disordered and amorphous carbon, Phys. Rev. B 61 (2001) 14095–14107, https://doi.org/10.1103/PhysRevB.61.14095.
[65] L.M. Malard, M.A. Pimenta, G. Dresselhaus, M.S. Dresselhaus, Raman spectroscopy in graphene, Phys. Rep. 473 (2009) 51–87, https://doi.org/10.1016/j.physrep.2009.02.003.
[66] M.A. Pimenta, G. Dresselhaus, M.S. Dresselhaus, L.G. Cançado, A. Jorio, R. Saito, Studying disorder in graphite-based systems by Raman spectroscopy, Phys. Chem. Chem. Phys. 9 (2007) 1276–1291, https://doi.org/10.1039/B613962K.
[67] S. Santangelo, Controlled surface functionalisation of carbon nanotubes by nitric acid vapors generated from sub-azeotropic solution, Surf. Interface Anal. 48 (2016) 17–25, https://doi.org/10.1002/sia.5875.
[68] S. Santangelo, M. Lanza, C. Milone, Evaluation of the overall crystalline quality of amorphous carbon containing multi-walled nanotubes, J. Phys. Chem. C 117 (2013) 4815–4823, https://doi.org/10.1021/jp310014w.
[69] Y. Li, S. Xu, X. Wu, J. Yu, Y. Wang, Y.S. Hu, X. Huang, Amorphous monodispersed hard carbon micro-spherules derived from biomass as a high performance negative electrode material for sodium-ion batteries, J. Mater. Chem. A 3 (2015) 71–77, https://doi.org/10.1039/C4TA05451B.

[70] C. Greco, U. Cosentino, D. Pitea, G. Moro, S. Santangelo, S. Patanè, M. D'Arienzo, M. Fiore, F. Morazzoni, R. Ruffo, Role of the carbon defects in the oxygen reduction by graphite nanoparticles: a spectromagnetic, electrochemical and computational integrated approach, Phys. Chem. Chem. Phys. 21 (2019) 6021–6032, https://doi.org/10.1039/C8CP07023G.
[71] K. Bogdanov, A. Fedorov, V. Osipov, T. Enoki, K. Takai, T. Hayashi, V. Ermakov, S. Moshkalev, A. Baranov, Annealing-induced structural changes of carbon onions: high-resolution transmission electron, microscopy and Raman studies, Carbon 73 (2014) 78–86, https://doi.org/10.1016/j.carbon.2014.02.041.
[72] Y. Wang, Q. He, H. Qu, X. Zhang, J. Guo, J. Zhu, S. Bhana, Magnetic graphene oxide nanocomposites: nanoparticles growth mechanism and property analysis, J. Mater. Chem. C 2 (2014) 9478–9488, https://doi.org/10.1039/C4TC01351D.
[73] H. Bi, K.C. Kou, K. Ostrikov, J.Q. Zhang, Graphitization of nanocrystalline carbon microcoils synthesized by catalytic chemical vapor deposition, J. Appl. Phys. 104 (2008) 033510(7p), https://doi.org/10.1063/1.2963712.
[74] Z. Lin, Y. Liu, Y. Yao, O.J. Hildreth, Z. Li, K. Moon, C. Wong, Superior capacitance of functionalized graphene, J. Phys. Chem. C 115 (2011) 7120–7125, https://doi.org/10.1021/jp2007073.
[75] W. Huang, Y. Zhang, S. Bao, S. Song, Desalination by capacitive deionization with carbon-based materials as electrode: a review, Surf. Rev. Lett. 20 (2013) 1330003 (10p), https://doi.org/10.1142/S0218625X13300050.
[76] H. Murphy, P. Papakonstantinou, T.T. Okpalugo, Raman study of multiwalled carbon nanotubes functionalized with oxygen groups, J. Vac. Sci. Technol. B 24 (2006) 715–720, https://doi.org/10.1116/1.2180257.
[77] D. Zhang, Q. Sun, Structure and properties development during the conversion of polyethylene precursors to carbon fibers, J. Appl. Polym. Sci. 62 (1996) 367–373, https://doi.org/10.1002/(SICI)1097-4628(19961010)62:2<367::AID-APP11>3.0.CO;2-Z.
[78] A. Morais, J.P.C. Alves, F.A.S. Lima, M. Lira-Cantu, A.F. Nogueira, Enhanced photovoltaic performance of inverted hybrid bulk-heterojunction solar cells using TiO2/reduced graphene oxide films as electron transport layers, J. Photonics for Energy 5 (2015) 057408(21p), https://doi.org/10.1117/1.JPE.5.057408.
[79] H.M. Wu, S.A. Chen, Dopant-polymer interaction: WCl6-doped polyacetylene, Synth. Met. 20 (1987) 169–183, https://doi.org/10.1016/0379-6779(87)90556-X.
[80] M. Rybachuk, J.M. Bell, Electronic states of trans-polyacetylene, poly (p-phenylene vinylene) and sp-hybridised carbon species in amorphous hydrogenated carbon probed by resonant Raman scattering, Carbon 47 (2009) 2481–2490, https://doi.org/10.1016/j.carbon.2009.04.049.
[81] G. Polzonetti, A.M. Cianciusi, A. Furlani, M.V. Russo, Photoelectron spectroscopy study of FeCl3 doped polyphenylacetylene, Synth. Met. 28 (1989) D413–D417, https://doi.org/10.1016/0379-6779(89)90723-6.
[82] M. Ding, F.H. Du, B. Liu, Z.Y. Leong, L. Guo, F. Chen, H.Y. Yang, Rod-like nitrogen-doped carbon hollow shells for enhanced capacitive deionization, Flat. Chem. 7 (2018) 10–17, https://doi.org/10.1016/j.flatc.2018.01.002.
[83] W. Shi, H. Li, X. Cao, Z.Y. Leong, J. Zhang, T. Chen, H. Zhang, H.Y. Yang, Ultrahigh performance of novel capacitive deionization electrodes based on a three-dimensional graphene architecture with nanopores, Sci. Rep. 6 (2015) 18996, https://doi.org/10.1038/srep18966 (9pp).
[84] G. Wang, L. Zhang, J. Zhang, A review of electrode materials for electrochemical supercapacitors, Chem. Soc. Rev. 41 (2012) 797–828, https://doi.org/10.1039/C1CS15060J.
[85] S. Patanè, C. Triolo, P. Cardiano, S. Lo Schiavo, Capacitive properties of the hydrophobic [2-(methacryloyloxy)ethyl]-trimethyl ammonium nonafluoro-1-butanesulfonate poly(ionic liquid) thin film, Ionics 23 (2017) 1481–1487, https://doi.org/10.1007/s11581-017-1971-7.
[86] T. Rath, P.P. Kundu, Reduced graphene oxide paper based nanocomposites materials for flexible supercapacitor, RSC Adv. 5 (2015) 26666–26674, https://doi.org/10.1039/C5RA00563A.
[87] D. Zhang, X. Zhang, Y. Chen, P. Yu, C. Wang, Y. Ma, Enhanced capacitance and rate capability of graphene/polypyrrole composite as electrode material for supercapacitors, J. Power Sources 196 (2011) 5990–5996, https://doi.org/10.1016/j.jpowsour.2011.02.090.
[88] B.A. Mei, O. Munteshari, J. Lau, B. Dunn, L. Pilon, Physical interpretations of Nyquist plots for EDLC electrodes and devices, J. Phys. Chem. C 122 (2018) 194–206, https://doi.org/10.1021/acs.jpcc.7b10582.
[89] J. Ma, L. Wang, F. Yu, Water-enhanced performance in capacitive deionization for desalination based on graphene gel as electrode material, Electrochim. Acta 263 (2018) 40–46, https://doi.org/10.1016/j.electacta.2018.01.041.
[90] T. Kim, J. Yoon, Relationship between capacitance of activated carbon composite electrodes measured at a low electrolyte concentration and their desalination performance in capacitive deionization, J. Electroanal. Chem. 704 (2013) 169–174, https://doi.org/10.1016/j.jelechem.2013.07.003.
[91] Z. Zhou, T. Liu, A.U. Khan, G. Liu, Block copolymer–based porous carbon fibers, Sci. Adv. 5 (2019) eaau6852, , https://doi.org/10.1126/sciadv.aau6852.
[92] C.M. Ghimbeu, J. Górka, V. Simone, L. Simonin, S. Martinet, C. Vix-Guterl, Insights on the Na+ ion storage mechanism in hard carbon: discrimination between the porosity, surface functional groups and defects, Nano Energy 44 (2018) 327–335, https://doi.org/10.1016/j.nanoen.2017.12.013.
[93] R. Yuksel, B. Yarar Kaplan, E. Bicer, A. Yurum, S. Alkan Gursel, H.E. Unalan, All-carbon hybrids for high performance supercapacitors, Int. J. Energy Res. 42 (2018) 3575–3587, https://doi.org/10.1002/er.4103.
[94] J. Niu, R. Shao, M. Liu, J. Liang, Z. Zhang, M. Dou, Y. Huang, F. Wang, Porous carbon electrodes with battery-capacitive storage features for high performance Li-ion capacitors, Energy Storage Mater. 12 (2018) 145–152, https://doi.org/10.1016/j.ensm.2017.12.012.
[95] S. Huo, Y. Zhao, M. Zong, B. Liang, X. Zhang, I.U. Khan, X. Song, K. Li, Boosting supercapacitor and capacitive deionization performance of hierarchically porous carbon by polar surface and structural engineering, J. Mater. Chem. A 8 (2020) 2505, https://doi.org/10.1039/C9TA12170F.
[96] G. Moussa, C.M. Ghimbeu, P.L. Taberna, P. Simon, C. Vix-Guterl, Relationship between the carbon nano-onions (CNOs) surface chemistry/defects and their capacitance in aqueous and organic electrolytes, Carbon 105 (2016) 628–637, https://doi.org/10.1016/j.carbon.2016.05.010.
[97] X. Yao, Y. Ke, W. Ren, X. Wang, F. Xiong, W. Yang, M. Qin, Q. Li, L. Mai, Defect-rich soft carbon porous nanosheets for fast and high-capacity sodium-ion storage, Adv. Energy Mater. 9 (2019) 1803260, https://doi.org/10.1002/aenm.201803260.
[98] C. Bommier, T.W. Surta, M. Dolgos, X. Ji, New mechanistic insights on Na-ion storage in nongraphitizable carbon, Nano Lett. 15 (2015) 5888–5892, https://doi.org/10.1021/acs.nanolett.5b01969.
[99] X. Guo, Y. Xue, H. Zhou, Y.X. Weng, J. Zhou, Achieving slope-reigned Na-ion storage in carbon nanofibers via constructing defect-rich texture by a Cu-activation strategy, ACS Appl. Mater. Interfa. 12 (2020) 2407–2416, https://doi.org/10.1021/acsami.9b17610.
[100] Y. Qi, Y. Lu, F. Ding, Q. Zhang, H. Li, X. Huang, L. Chen, Y.S. Hu, Slope-dominated carbon anode with high specific capacity and superior rate capability for high safety Na-ion batteries, Angew. Chem. 131 (2019) 4405–4409, https://doi.org/10.1002/ange.201900005.
[101] P.A. Denis, F. Iribarne, Comparative study of defect reactivity in graphene, J. Phys. Chem. C 117 (2013) 19048–19055, https://doi.org/10.1021/jp4061945.
[102] D.E. Jiang, B.G. Sumpter, S. Dai, Unique chemical reactivity of a graphene nanoribbon's zigzag edge, J. Chem. Phys. 126 (2007) 134701, https://doi.org/10.1063/1.2715558.
[103] S. Ardizzone, G. Fregonara, S. Trasatti, "Inner" and "outer" active surface of RuO2 electrodes, Electrochim. Acta 35 (1990) 263–267, https://doi.org/10.1016/0013-4686(90)85068-X.
[104] O.I. Malyi, K. Sopiha, V.V. Kulish, T.L. Tan, S. Manzhos, C. Persson, A computational study of Na behavior on graphene, Appl. Surf. Sci. 333 (2015) 235–243, https://doi.org/10.1016/j.apsusc.2015.01.236.
[105] H. Li, Y. Gao, L. Pan, Y. Zhang, Y. Chen, Z. Sun, Electrosorptive desalination by carbon nanotubes and nanofibres electrodes and ion-exchange membranes, Water Res. 42 (2008) 4923–4928, https://doi.org/10.1016/j.watres.2008.09.026.
[106] H. Zhang, P. Liang, Y. Bian, Y. Jiang, X. Sun, C. Zhang, X. Huang, F. Wei, Moderately oxidized graphene – carbon nanotubes hybrid for high performance capacitive deionization, RSC Adv. 6 (2016) 58907–58915, https://doi.org/10.1039/C6RA10088K.
[107] Y. Wimalasiri, L. Zou, Carbon nanotube/graphene composite for enhanced capacitive deionization performance, Carbon 59 (2013) 464–471, https://doi.org/10.1016/j.carbon.2013.03.040.
[108] X. Gu, M. Hu, Z. Du, J. Huang, C. Wang, Fabrication of mesoporous graphene electrodes with enhanced capacitive deionization, Electrochim. Acta 182 (2015) 183–191, https://doi.org/10.1016/j.electacta.2015.09.076.
[109] P. Liu, H. Wang, T. Yan, J. Zhang, L. Shi, D. Zhang, Grafting sulfonic and amine functional groups on 3D graphene for improved capacitive deionization, J. Mater. Chem. A 4 (2016) 5303–5313, https://doi.org/10.1039/C5TA10680J.
[110] W. Kong, X. Duan, Y. Ge, H. Liu, J. Hu, X. Duan, Holey graphene hydrogel with in-plane pores for high-performance capacitive desalination, Nano Res. 9 (2016) 2458–2466, https://doi.org/10.1007/s12274-016-1132-8.
[111] G. Zhu, H. Wang, H. Xu, L. Zhang, Enhanced capacitive deionization by nitrogen-doped porous carbon nanofiber aerogel derived from bacterial-cellulose, J. J. Electroanal. Chem. 822 (2018) 81–88, https://doi.org/10.1016/j.jelechem.2018.05.024.
[112] J. Kim, J. Kim, J.H. Kim, H.S. Park, Hierarchically open-porous nitrogen-incorporated carbon polyhedrons derived from metal-organic frameworks for improved CDI performance, Chem. Eng. J. 382 (2020) 122996, https://doi.org/10.1016/j.cej.2019.122996.
[113] Q. Dong, G. Wang, B. Qian, C. Hu, Y. Wang, J. Qiu, Electrospun composites made of reduced graphene oxide and activated carbon nanofibers for capacitive deionization, Electrochim. Acta 137 (2014) 388–394, https://doi.org/10.1016/j.electacta.2014.06.067.
[114] L. Wang, M. Wang, Z.H. Huang, T. Cui, X. Gui, F. Kang, K. Kang, D. Wu, Capacitive deionization of NaCl solutions using carbon nanotube sponge electrodes, J. Mater. Chem. 21 (2011) 18295–18299, https://doi.org/10.1039/C1JM13105B.